AD-A194 265 FELLOWSHIPS IN HYPERSONIC AERODYNAMICS(U) MARYLANDUUNIV 1/1
COLLEGE PARK DEPT OF AEROSPACE ENGINEERING
J D ANDERSON FEB 88 ARO-20252 2-EG-F DAAG29-83-G-0018
UNCLASSIFIED F/G 20/4 NL

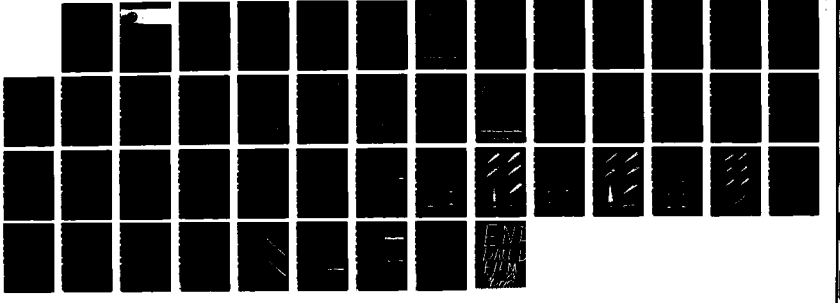

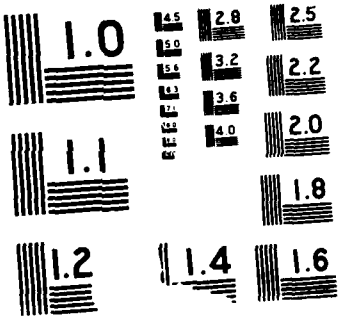
1.0
1.1
1.2
1.4
1.6
1.8
2.0
2.2
2.5
2.8
3.2
3.6
4.0
4.5
5.0

University of Maryland, College Park
Department of Aerospace Engineering

FELLOWSHIPS IN HYPERSONIC AERODYNAMICS

FINAL REPORT

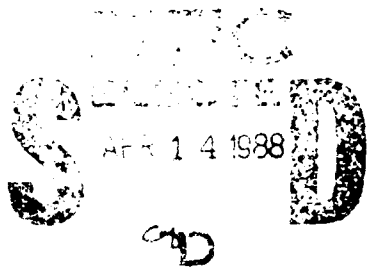

by

John D. Anderson, Jr.

February, 1988

U.S. ARMY RESEARCH OFFICE

GRANT DAAG-29-83-G-0018

Department of Aerospace Engineering
University of Maryland
College Park, Maryland 20742

FELLOWSHIPS IN HYPERSONIC AERODYNAMICS

FINAL REPORT

by

John D. Anderson, Jr.

February, 1988

U.S. ARMY RESEARCH OFFICE

GRANT DAAG-29-83-G-0018

Department of Aerospace Engineering
University of Maryland
College Park, Maryland 20742

MASTER COPY - FOR REPRODUCTION PURPOSES

UNCLASSIFIED
SECURITY CLASSIFICATION OF THIS PAGE (When Data Entered)

REPORT DOCUMENTATION PAGE		READ INSTRUCTIONS BEFORE COMPLETING FORM
1. REPORT NUMBER	2. GOVT ACCESSION NO. N/A	3. RECIPIENT'S CATALOG NUMBER N/A
4. TITLE (and Subtitle) FELLOWSHIPS IN HYPERSONIC AERODYNAMICS		5. TYPE OF REPORT & PERIOD COVERED Final 3/1/83-8/31/86
		6. PERFORMING ORG. REPORT NUMBER
7. AUTHOR(s) John D. Anderson, Jr.		8. CONTRACT OR GRANT NUMBER(s) DAAG-29-83-G-0018
9. PERFORMING ORGANIZATION NAME AND ADDRESS Department of Aerospace Engineering University of Maryland College Park, Maryland 20742		10. PROGRAM ELEMENT, PROJECT, TASK AREA & WORK UNIT NUMBERS
11. CONTROLLING OFFICE NAME AND ADDRESS U. S. Army Research Office Post Office Box 12211 Research Triangle Park, NC 27709		12. REPORT DATE February 1988
		13. NUMBER OF PAGES 30
14. MONITORING AGENCY NAME & ADDRESS(if different from Controlling Office)		15. SECURITY CLASS. (of this report) Unclassified
		15a. DECLASSIFICATION/DOWNGRADING SCHEDULE

16. DISTRIBUTION STATEMENT (of this Report)

Approved for public release; distribution unlimited.

17. DISTRIBUTION STATEMENT (of the abstract entered in Block 20, if different from Report)

NA

18. SUPPLEMENTARY NOTES

The view, opinions, and/or findings contained in this report are those of the author(s) and should not be construed as an official Department of the Army position, policy, or decision, unless so designated by other documentation.

19. KEY WORDS (Continue on reverse side if necessary and identify by block number)

Hypersonic aerodynamics, waveriders, hypersonic vehicles, Viscous Hyper... Axi...

20. ABSTRACT (Continue on reverse side if necessary and identify by block number)

This fellowship program supported two Ph.D. students in hypersonic aerodynamics. The research was carried out in two categories: (1) The study of hypersonic waveriders, and the generation of a family of optimized waveriders including viscous effects; (2) The numerical study of the interaction of a shock wave and a vortex at hypersonic speeds. Here, the calculations were made using a finite-volume technique with upwind differencing. Hyper...

DD FORM 1 JAN 73 1473 EDITION OF 1 NOV 65 IS OBSOLETE

UNCLASSIFIED
SECURITY CLASSIFICATION OF THIS PAGE (When Data Entered)

I. INTRODUCTION

This is a final report on a three-year fellowship program in hypersonic aerodynamics sponsored at the University of Maryland by the Army Research Office. This program was initiated in March 1983, and was an insightful precurser to the massive activity in hypersonic aerodynamics now sweeping the country. This ARO fellowship program was characterized by the following:

(1) It was the first fellowship program in hypersonic aerodynamics in any university.

(2) It helped to spark a research activity in hypersonic aerodynamics at the University of Maryland--an activity that now encompasses 12 full-time graduate students.

(3) It sponsored two exceptional Ph.D. students--both straight A students--with fellowships in hypersonic aerodynamics for three years.

(4) One of these students, Dr. Kevin Bowcutt, graduated in August 1986. He has since gone on to distinguish himself as a leader in the National Aerospace Plane program at Rockwell International.

(5) The other student is Griffin Corpening, who will graduate in May 1988. Mr. Corpening is presently working at the Johns Hopkins Applied Physics Laboratory in their hypersonic vehicle program.

In light of the above, the ARO Fellowship Program in Hypersonic Aerodynamics has had a synergestic effect, not only at Maryland, but on the national hypersonic program in the United States far beyond the initial expectations for the program.

In the following, the research conducted under this fellowship program is summarized.

II. VISCOUS OPTIMIZED HYPERSONIC WAVERIDERS

Here the research is summarized by two AIAA papers, reproduced in total on the following pages. One paper, by Bowcutt and Anderson, represents work totally sponsored by ARO, and is derived from the Ph.D. dissertation of Kevin Bowcutt. This paper is self-explanatory. The second paper, by Corda and Anderson, represents a derivation of the ARO sponsored work, and is included here to demonstrate the synergestic effect of this grant.

AIAA'88

AIAA-88-0369
Viscous Optimized Hypersonic Waveriders Designed from Axisymmetric Flow Fields

S. Corda and J. D. Anderson, Jr.,
University of Maryland, College Park, MD

AIAA 26th Aerospace Sciences Meeting
January 11-14, 1988/Reno, Nevada

VISCOUS OPTIMIZED HYPERSONIC WAVERIDERS DESIGNED FROM AXISYMMETRIC FLOW FIELDS

by

Stephen Corda* and John D. Anderson, Jr.**

Department of Aerospace Engineering
University of Maryland
College Park, Maryland 20742

ABSTRACT

A series of "viscous optimized" waveriders is designed from general axisymmetric flow fields, other than conical -- most notibly, flow fields over minimum drag bodies. These configurations represent the next logical step in an ongoing program of research on the design of hypersonic waveriders at the University of Maryland. In previous work at Maryland, inviscid conical flow was used exclusively in the design of waveriders. These conical flow waveriders predict high values of lift/drag, higher than the values based on experience from other hypersonic configurations. The present work allows the design of hypersonic waveriders from any axisymmetric flow field -- although the present results focus on the inviscid flows over cones and 3/4 and 1/2 power-law bodies. A space marching, finite-difference code is used to generate the axisymmetric flow field. The undersurface of the vehicle is carved out as a stream surface of this axisymmetric flow field, whereas the upper surface is assumed to be a freestream surface. The detailed viscous effects are included within the optimization process, using a simple reference temperature method. Results obtained using the reference temperature method are within 10% of results obtained using a more complex integral boundary layer method, even at high hypersonic Mach numbers. Boundary layer transition is predicted using a correlation of the local transition Reynolds number with the Mach number. A non-linear simplex method is used to optimize the waveriders for either maximum L/D or minimum total drag.

INTRODUCTION

In recent years, research involving all aspects of hypersonic flight has seen a rebirth in the United States. An extended survey of hypersonic aerodynamic research is given in Reference 1. During the long hiatus that hypersonic research lay dormant, powerful new engineering tools have become available -- i.e. supercomputers and computational fluid dynamics (CFD). In fact, vehicle concepts such as the National Aerospace Plane (NASP), aero-assisted orbital transfer vehicles (AOTV's), the hypersonic transport (the "Orient Express"), and hypersonic missiles, place much of the design burden upon CFD. In addition, advanced computers and computational techniques allow us to take a "new" look at some "old" hypersonic aerodynamic concepts. The present paper is part of a continuing hypersonics research program, at the University of Maryland, that does just that. Using modern computational techniques, the "old" concept of waveriders is revisited to produce a "new" class of advanced hypersonic lifting configurations. This CFD approach to the waverider concept has lead to a design tool with the following "new" advantages:

1. The waverider configurations can be numerically optimized for almost any figure of merit -- maximum L/D and minimum total drag, in the present study.

2. The detailed viscous effects are included within the optimization process.

3. The waverider configurations can be carved out as stream surfaces of almost any axisymmetric flow field -- the inviscid flow over cones and 3/4 and 1/2 power-law bodies are used in the present investigation.

4. Even with the above detailed effects and versatility, the waverider optimization procedure is computational efficient, allowing parametric design studies to be made.

The advantages listed above will be elaborated upon in the paragraphs to come.

This paper is a sequel to Reference 2. In References 2 and 3, Bowcutt and Anderson established a new class of hypersonic vehicles that broke the "L/D barrier" as depicted in Figure 1. This barrier represents a general empirical correlation for $(L/D)_{max}$, as the freestream Mach number, M_∞, increases across the supersonic and hypersonic regimes, based on actual flight vehicle experience. It is given by the relation

$$(L/D)_{max} = \frac{4(M_\infty + 3)}{M_\infty}$$

(obtained from Reference 4), and is shown by the solid line in Figure 1. A number of data points

---

* Graduate Research Assistant, Student Member, AIAA.

** Professor of Aerospace Engineering, Fellow, AIAA.

for optimized waveriders generated by Bowcutt and Corda are shown along with various other hypersonic configurations at various Reynolds numbers and Mach numbers. (The points on this graph correspond to different references as given in References 5 and 6.) The waveriders generated by Bowcutt are seen to follow the relation given by

$$(L/D)_{max} = \frac{5(M_\infty + 2)}{M_\infty}$$

shown by the dashed curve in Figure 1. The present waverider results, as represented by the solid circles in Figure 1, will be discussed in subsequent sections.

To fully appreciate the logical sequence of the present waverider research and how it represents a contribution to the state-of-the-art, let us review the fundamental concepts of waveriders. In 1959, Nonweiler[7] proposed the idea of constructing a three-dimensional hypersonic vehicle from a known flow field. Nonweiler chose the flow field behind a planar oblique shock wave to generate a class of vehicles with a caret-shaped cross-section and a delta planform. The construction of a caret wing, as they are called, is shown in Figure 2 (from Reference 8). When flying at its design Mach number, the body appears to be riding on top of the attached shock wave, and hence is dubbed a "waverider". There is no flow spillage from the lower to the upper surface of the vehicle when it is flying at its design Mach number because the shock wave is attached to the leading edges. This containment of the flow beneath the vehicle results in high pressure being exerted on the lower surface -- the high pressure behind the two-dimensional planar shock wave. This high pressure leads to high lift. It can be stated that, in general, when compared at the same lift coefficient, caret wings have higher values of L/D than other winged hypersonic vehicles. The aerodynamic benefits of waveriders are listed in Reference 1, and are discussed in detail in References 5, 6, and 9.

The idea of generating a three-dimensional hypersonic vehicle from a known flow field can be extended from Nonweiler's construction (which uses a simple two-dimensional wedge) to more complex flows. For example, a conical flow can be used, as shown in Figure 3 (from Reference 8). The resulting class of "conical-flow" waveriders was first investigated by the British (see Reference 10). Rasmussen et al.[11,12], Cole and Zien[13], and Kim et al.[14] represent further variations -- designing waveriders from flows over cones and elliptic cylinders using hypersonic small disturbance theory. Further, these investigators used the calculus of variations to search for optimum waverider shapes. Bowcutt and Anderson[2,3] generated a series of conical-flow waveriders that were numerically optimized for maximum L/D. Unlike previous investigators, they are the first to include the detailed viscous effects (including boundary layer transition) within the optimization process. This helps to alleviate a fundamental drawback of waveriders -- the large friction drag associated with a waverider's characteristically large wetted area. With skin friction effects fully accounted for within the optimization procedure, a configuration can be found which balances the desire for aerodynamic efficiency (high L/D) with the large wetted area (hence high friction drag) attendent with this high L/D.

The present work takes the next logical step, going beyond conical flow fields, to generate "viscous optimized" waveriders from general axisymmetric flow fields -- most notibly, flow over minimum drag bodies. Again, the detailed viscous effects are included within the optimization process. The rationale behind this direction is as follows. One might intuitively suspect that the flow over a minimum drag power-law body might lead to waveriders of lower drag and higher L/D than those derived from conical flow, by nature of the generating flow field itself. The need for minimum drag and high L/D are of paramount importance for vehicles (such as the aerospace plane) that must be able to accelerate and cruise as efficiently as possible. One might also expect a better volume distribution (meaning more volume in the nose of the vehicle for packaging of payload or avionics) with a power-law derived waverider than with a conically derived waverider. In particular, the present results show waveriders designed from the flow over cones and 1/2 and 3/4 power-law bodies. Also, the configurations are numerically optimized, using the non-linear simplex method of Nelder and Mead[15], for maximum L/D and for minimum total drag.

ANALYSIS

The analysis and optimization of waveriders from general axisymmetric flow fields require distinct capabilities. First, one must be able to generate a "known" axisymmetric flow field. Then one must analyze the waverider generated from the flow field which involves: 1) the evaluation of the aerodynamic coefficients (e.g. C_L, C_D, and C_M) and 2) the determination of the parameters which describe the waverider geometry. Finally, waverider optimization requires finding the set of parameters that yield the desired figure of merit (e.g. maximum L/D or minimum C_D). The breakdown of the waverider design process is shown in Figure 4. The contents of each box will be discussed in the following paragraphs. A more detailed description of the design process is given in Reference 6.

A. Generation of Inviscid Flow Field

The calculation of the "known" axisymmetric flow field will be discussed first. Separate techniques are used for the case of 1) flow over a right circular cone and 2) flow over a general axisymmetric body, as described below.

A.1 Conical Flow

For the case of conical flow, the ordinary differential equation know as the Taylor-Maccoll equation is solved using a standard fourth-order Runge-Kutta method as given in Reference 16 and shown below.

$$\frac{\gamma-1}{2}\left[1-V_r^2-\left(\frac{dV_r}{d\theta}\right)^2\right]\left[2V_r+\frac{dV_r}{d\theta}\cot\theta+\frac{d^2V_r}{d\theta^2}\right]$$

$$-\frac{dV_r}{d\theta}\left[V_r\frac{dV_r}{d\theta}+\frac{dV_r}{d\theta}\frac{d^2V_r}{d\theta^2}\right]=0 \qquad (1)$$

In equation (1), V_r is the nondimensional component of flow velocity along a conical ray, θ is the angle of the ray referenced to the cone axis, and γ is the ratio of specific heats.

A2. General Axisymmetric Flow Field

For an inviscid axisymmetric flow field in general, the governing partial differential equations are the Euler equations given below

$$\frac{\partial G}{\partial z} = -\frac{\partial E}{\partial r} - H \qquad (2)$$

$$G=\begin{bmatrix}\rho w\\ p+\rho w^2\\ \rho vw\end{bmatrix}$$

$$E=\begin{bmatrix}\rho v\\ \rho vw\\ p+\rho v^2\end{bmatrix}$$

$$H=\frac{1}{r}\begin{bmatrix}\rho v\\ \rho vw\\ \rho v^2\end{bmatrix}$$

where ρ is the density, w is the axial (z) component of the flow velocity, v is the transverse (r) component of the flow velocity, and p is the pressure.

These equations are solved numerically using MacCormack's explicit, space-marcing, finite-difference scheme. In this technique, the flow field of interest is discretized into a network of grid points in the axial (z) and radial (r) directions. Starting from an initial data plane, where the flow properties are assumed known, the flow field solution is calculated by marching downstream in steps of Δz. The shock-fitted approach is used where the solution is bounded by the surface of the body and the shock wave produced by the body. Applied to the Euler equations, the scheme can be written as

$$\overline{G_j^{n+1}} = G_j^n - \frac{\Delta z}{\Delta r}\left(E_{j+1}^n - E_j^n\right) - \Delta z\, H_j^n \qquad (3a)$$

$$G_j^{n+1} = \frac{1}{2}\left(G_j^n + \overline{G_j^{n+1}} - \frac{\Delta z}{\Delta r}\left(\overline{E_j^{n+1}} - \overline{E_{j-1}^{n+1}}\right) - \Delta z\,\overline{H_j^{n+1}}\right) \qquad (3b)$$

where Δz is the marching increment in the axial (z) direction, Δr is the distance between grid points in the radial (r) direction, n is the grid point index in the axial direction, and j is the grid point index in the radial direction. To obtain a stable solution, the downstream marching is limited by the CFL criterion

$$\Delta z = C\,\frac{\Delta r}{\tan(\theta+\mu)} \qquad (4)$$

where C is a constant between 0 and 1. A value of C equal to 0.95 is used in all of the calculations presented in this paper.

As mentioned earlier, the flow field solution is started from a known data line. For this reason, the body of interest is assumed to have a conical nosetip. The flow field behind the conical nosetip is solved using the Taylor-Maccoll cone flow solution outlined in the previous section. This nosetip flow field is then matched with the body of interest to serve as an initial data line for the space-marching solution. For a detailed account of MacCormack's space-marching technique, including the application of the boundary conditions, see References 6 or 17.
body of interest to serve as an initial data line for the space-marching solution. For a detailed account of MacCormack's space-marching technique, including the application of the boundary conditions, see References 6 or 17.

B. Generation of Leading Edge Shapes

Once the flow field is calculated, waverider shapes can be "carved" out of the flow field as shown in Figure 5. As is seen in this figure, the leading edge curve is traced back along the streamlines of the flow field to generate the lower surface of a waverider. Note that the projection of the leading edge curve in the cross-stream (x-y) plane uniquely defines a waverider geometry for a given flow field. The leading edge curves are generated by the optimization process as will be discussed shortly.

C. Streamline Tracing

As noted in the previous section, streamlines are traced from the leading edge, through the "known" flow field, to create the waverider lower surface. The manner of this streamline tracing will now be described.

From the space-marching solution, flow properties are known at distinct axial (z) stations. Tracing a streamline amounts to finding where the value of the streamfunction, ψ, along each z data line is equal to the value of the streamfunciton of the specified streamline. The streamfunction along each data line can be calculated by using the definition of the streamfunction for an axially symmetric flow.

$$\psi_{j+1} = \psi_j + \dot{m} \qquad (5)$$

where ψ is the value of the streamfunction, j is a radial (r) index for data points along a z station, and $\dot{m}$ is the mass flow in the annulus bounded by the points j and j+1. By setting the value of the streamfunction at the body surface equal to zero, the value of the streamfunction can be calculated along each z data line.

D. Freestream Upper Surface

The generation of the waverider lower surface by streamline tracing has been described in the previous sections. The upper surface is created by simply following the freestream back through the given leading edge curve to the base of the waverider. The pressure on this freestream upper surface is the freestream pressure, p_∞.

E. Skin Friction Calculations

The skin friction distribution along the streamlines that form the waverider is calculated using the reference temperature method of Eckert[19]. In the reference temperature method, approximate formulas are used to predict the skin friction, with the physical properties evaluated at an appropriate reference temperature. For a flat plate in laminar flow, the local skin friction coefficient is given by

$$c_f = 0.664\ (Re_x)^{-1/2}\ (T'/T_\infty)^{(\omega-1)/2} \qquad (6)$$

Re_x is the local Reynolds number defined as

$$Re_x = \frac{\rho_\infty V_\infty x}{\mu_\infty} \qquad (7)$$

where ρ_∞ is the freestream density, V_∞ is the freestream velocity, x is the local distance from the leading edge of the plate, and μ_∞ is the freestream value of the viscosity.

Also in equation (6), T' is the reference temperature defined as

$$(T'/T_\infty) = 1 + 0.032\ M_\infty^2 + 0.58\ (T_w/T_\infty - 1) \qquad (8)$$

where M_∞ is the freestream Mach number and T_w is the wall temperature. Finally, ω in equation (6) is the exponent of an assumed exponential variation of μ, namely,

$$(\mu'/\mu_\infty) = (T'/T_\infty)^\omega \qquad (9)$$

A value of $\omega = 0.75$ is used in the present study.

The flat plate skin friction coefficient for turbulent flow is given by

$$c_f = \frac{0.0592}{(Re_x')^{0.2}} \qquad (10a)$$

where

$$Re_x' = \frac{\rho' V_\infty x}{\mu'} \qquad (10b)$$

In equation (10b), ρ' and μ' are evaluated at the reference temperature T'.

This type of skin friction analysis is much simpler, in concept and use, than integral boundary layer methods (such as used in Reference 2). Results obtained using the reference temperature method were within 10% of results using a more complex integral boundary layer method (Reference 2), even at high hypersonic Mach numbers. Also, the computation time required by the reference temperature method is very small when compared with an integral boundary layer method.

Boundary layer transition is predicted using a correlation of the local transition Reynolds number, $Re_{x,t}$ with the local edge Mach number, M_e, as follows

$$\log_{10} Re_{x_t} = 6.421\ e^{(1.209\times10^{-4} M_e^{2.641})} \qquad (11)$$

This correlation is the same as used in the previous work by Bowcutt and Anderson[2,3] and is based on the experimental data of DiCristina[19] for transition on sharp cones at zero degrees angle of attack. This correlation is used due to the lack of better methods of transition prediction in hypersonic flows.

F. Aerodynamic Forces and Moments

The aerodynamic force and moment coefficients are calculated by numerically integrating the pressure and shear stress over the surface of the waverider. Base drag is not calculated. Details of the integration for the forces and moments can be found in Reference 6.

G. Waverider Optimization

The construction and aerodynamic analysis of a single waverider configuration is shown by blocks A through F, in Figure 4, and just described in the previous paragraphs. Now, the optimization is performed by perturbing the shape of the leading edge curve (which corresponds to a unique waverider geometry), until a configuration is found with the optimum value of the specified figure of merit -- either maximum L/D or minimum total drag, in the present analysis. The non-linear simplex method of Nelder and Mead[15] is used for the numerical optimization. Because this is a zero order method, only function evaluations are needed to find an optimum (no derivative information is needed). These function evaluations are the determinations of the figure of merit (e.g. L/D or C_D) for each configuration. The zero order methods are the easiest to implement and it was shown by VanWie[20] that the non-linear simplex method worked as well as other higher-order methods when applied to a similar type of optimization problem as is considered here.

The non-linear simplex method minimizes a function of n variables by comparing values of the function at (n+1) vertices of a "simplex", replacing the vertex with the highest function value with another point determined by the logic of the scheme, and then "moving" this simplex, over the function surface, in the direction of the function minimum. Three operations are used by

the simplex in its search for the function minimum -- reflection, expansion, and contraction. These operations are graphically illustrated by considering the minimization problem shown in Figure 6. Here, the minimum of a function of two variables (X_1 and X_2) is sought, where the contour map defines the function. A simplex composed of n+1=3 vertices (a triangle) moves over the function surface by reflecting or "flip-flopping" down the function valley, expanding if possible to speed up the process, and finally contracting around the function minimum. Constraints in the optimization process take the form of "barriers" or boundaries that the simplex is not allowed to cross. The nature of these constraints will be discussed in a later section.

In the present work, the function to be minimized is the negative of the lift/drag ratio or the value of the total drag coefficient. Each function evaluation corresponds to a unique waverider configuration, which can be parameterized by its leading edge shape. Therefore, a leading edge curve represents a single vertex point of the simplex. The leading edge is specified by five points in the cross-stream (x-y) plane, where a cubic spline is used to define a smooth, continuous curve. It should be noted that calculations are performed for only half of the vehicle because of its longitudinal symmetry. One of the five points is constrained to lie on the symmetry plane (y-axis) of the waverider, thus reducing the number of x, y coordinates, needed to define the leading edge, from 10 to 9. The number of coordinate variables is further reduced to 8 by the constraint that the last leading edge point must lie on the shock wave. It is these eight variables that are perturbed by the logic of the optimization routine to find an optimum waverider.

Since the optimization problem is reduced to finding the minimum of a function defined by eight variables (n=8), the simplex for this problem has n+1 or nine vertices with each vertex corresponding to a set of coordinates for a leading edge curve. To initiate the simplex method, nine leading edge shapes must be chosen -- so-called basis leading edge shapes. In the present study, six of the basis leading edge shapes are polynomials of the form

$$y_{le} = C_1 + C_2 x_{le} + C_3 x_{le}^2 + C_4 x_{le}^3 \qquad (12)$$

and three of the basis shapes are of the forms

$$y_{le} = C_5 + C_6 \left(1 - \cos \frac{\pi x_{le}}{r_s}\right) \qquad (13a)$$

$$y_{le} = C_7 + C_8 \sin \left(\frac{\pi x_{le}}{r_s}\right) \qquad (13b)$$

where x_{le} and y_{le} are the x and y coordinates of the leading edge and r_s is the radius of the shock wave at the base of the waverider. A set of basis leading edge shapes is shown in Figure 7. The final optimized leading edge curve is also shown as the bold line in this figure. A typical optimization history is shown in Figure 8. In all of the results presented, 100 optimization steps or levels are used to reach an "optimium" waverider configuration.

III. RESULTS AND DISCUSSION

The presented results are representative of the work done in Reference 6. The following areas will be covered: (1) validation of the computer code used to construct and aerodynamically analyze a waverider (no optimization); (2) a presentation of optimum waveriders designed from conical and power-law body flow fields, over a wide range of hypersonic Mach numbers; (3) the comparison of waveriders optimized for maximum L/D with those optimized for minimum total drag; (4) the effect of using an all laminar, all turbulent, or transiting boundary layer in the waverider optimization; and (5) a word will be said concerning the computing time required.

A. Code Validation

Because of the unique design method used in the present analysis, it is impossible to find experimental data to confirm the computational results presented. However, certain point comparisons can be made. One such case is the hypersonic flow over a half-cone underneath a delta wing configuration at zero degrees angle of attack. Experiments by Fetterman[21] on a 4 degree semi-apex angle half-cone under a delta wing of 81 degrees sweepback closely approximate tests of a waverider configuration at a Mach number of 6.86. Table 1 summarizes the results of this comparison. The wall temperature of the model in the experiments is unknown, so calculations are made for a wall temperature equal to the freestream temperature and equal to the total temperature of the flow. Also, the model used in the experiment has a 1 degree compression on the upper surface of the delta wing from the leading edge to approximately the midchord position. It was not feasible to model this compression surface so calculations were made for a freestream upper surface and for a 1 degree compression on the entire upper surface. Table 1 shows that calculations of the lift coefficient, C_L, are in good agreement with experiment. The calculated values of the drag coefficient, C_D, for the freestream and 1 degree compression upper surface, bracket the experimental value as would be expected. This same trend follows through to the comparison of the lift/drag ratio.

Another source for comparison of the present results is the previous work by Bowcutt[2], for conical flows only. This is possible because all of the computational tools used in the present investigation were developed independently of this previous work. Indeed, for the case of conical flow waveriders, the present code and the previous code developed by Bowcutt differ by a few percent for most parameters of interest. For a Mach number equal to 6 and a cone angle of 12 degrees, the present code predicts an L/D of 7.34 and Bowcutt's code predicts an L/D of 7.73 -- a difference of about 5 percent. For a higher Mach number of 14, the values of the lift/drag ratio are 6.06 and 5.87 from Bowcutt's code and the present code respectively -- a difference of about 3 percent. This comparison also helps to validate the reference temperature method, used for the

viscous flow analysis in the present work, since Bowcutt's code used a much more complex integral boundary layer method. The comparison is especially encouraging at the higher Mach numbers where the accuracy of the reference temperature method may be suspect.

B. Waveriders Designed From Cones and Power-Law Bodies

Waveriders are optimized at specific design points (e.g. Mach number and altitude) along the possible flight trajectory of an aerospace plane. These design points are flight Mach numbers of 4, 6, 10, 14, and 20 with corresponding altitudes of 80,000, 110,000, 125,000, 140,000, and 175,000 feet. All calculations are for a calorically perfect gas.

The design of the waveriders are optimized under a set of geometric constraints that are easily specified by the program user. These constraints include the following:

1. A constraint on the lower limit of the slenderness ratio (reciprocal of the fineness ratio) of the waverider--equal to 0.075 times the length of the vehicle, in the present results.

2. Constraints on the box size (semi-span-to-length ratio) of the waverider--the lower limit is 0.1 and the upper limit is 0.4, in the present study.

3. A constraint on the minimum acceptable total volume of the vehicle -- not an active constraint for the present results.

A study was made to assess the effect of these constraints on the design process but will not be discussed here. Reference 6 can be consulted for complete details.

The present results are for waveriders designed from flow over cones and 1/2 and 3/4 power-law bodies. Typical body shapes are illustrated in Figure 9 for a Mach number of 10 and a base radius-to-length ratio, r_{base}/L, of 0.15. For a given Mach number and body type, the design strategy is as follows. A fineness ratio of the flow generating body is selected and the flow field corresponding to this body is calculated using either the Taylor-Maccoll solution (if the body is a cone) or the space-marching technique (if the body is a power-law body). The optimum waverider is then found for this flow field. Additional fineness ratios are selected and the optimum waverider corresponding to each of these flow fields is obtained. Figure 10 shows a series of waveriders optimized for maximum L/D for a Mach number of 6. Each one of the data points corresponds to a waverider that is optimized for a given fineness ratio of the flow field generating body, although the lift/drag ratio is plotted versus the fineness ratio of the waverider itself. From Figure 10, it is seen that there is an "optimum of the optimums" for each of the body types. In general, it is also evident that, for a given waverider fineness ratio, the waveriders designed from the 1/2 power-law body have the highest L/D, followed by those designed from the 3/4 power-law body and those designed from the cone.

All of the remaining results in this section are for waveriders that are optimized for maximum L/D. Figure 11 shows a plot of the lift/drag ratio versus the Mach number for waveriders that are the "optimum of the optimums". In general, the power-law derived waveriders have slightly higher values of L/D than the conically derived waveriders over the Mach number range shown. The waveriders designed from 1/2 power-law bodies are seen to be the best overall, in terms of high L/D. Also note that, for all the body types, the value of L/D decreases then increases with increasing Mach number. The waverider configurations designed from the 1/2 power-law body and the cone, for Mach numbers of 4 and 20, are shown in Figures 12 and 13.

Figure 14 shows a plot of the lift/drag ratio versus the lift coefficient, C_L, for the optimum waveriders discussed in the previous paragraph. Note that decreasing C_L in this figure corresponds to an increasing Mach number. Here, the power-law body derived waveriders generally predict higher values of L/D, for a given value of C_L, than the cone-derived waveriders. Again, note the decrease then increase in L/D as the value of C_L decreases (Mach number increasing).

Figure 15 shows L/D plotted against a Mach number times the fineness ratio of the flow generating body. This figure shows a reversal in trends, in terms of which flow field yields the waverider with the highest L/D. The power-law bodies are better at the lower values of $M_\infty(b/l_b)$, and the cones are better at higher values. Also, it is seen that the shapes of the curves in Figure 15 are similar for each type of flow field. This tends to suggest that the quantity $M_\infty(b/l_b)$ is a valid hypersonic similarity parameter for the type of waverider design process presented in this paper.

Returning to figure 1, note the symbols denoted by solid circles. These symbols correspond to the waveriders with the highest L/D, designed from the flow over 1/2 power-law bodies, at the various Mach numbers. Note that they also break the "L/D barrier" as described earlier. As described earlier, the data for L/D displays a "bucket" type behavior with increasing Mach number. The decrease then increase in the value of L/D, as Mach number increases, is a Reynolds number effect as discussed in Reference 2.

The total drag coefficient, C_D, is plotted against Mach number for the "optimum of the optimums" waveriders in Figure 16. The value of drag coefficient is seen to decrease with increasing Mach number for all of the flow types. Note that, except for the Mach 6 case, the cone-flow derived waveriders have the slightly higher values of drag coefficient. It is interesting to note, in Figure 17, the breakdown of drag, into wave and skin friction drag, for the 3/4 power-law body flow. It is seen that the skin friction drag and wave drag are nearly equal throughout the Mach number regime. These trends are true for the other flow field results.

Finally, Figure 18 shows volumetric efficiency, $V^{2/3}/S$ (where V is the total volume of the waverider and S is its planform area) versus Mach number for the optimum waveriders. This figure is shown to indicate the order of magnitude of the volumetric efficiency for the present class of waverider vehicles. In general, the power-law body derived waveriders appear to be more volume efficient than their conically derived counterparts, but the trend is not consistent.

C. Maximum L/D Versus Minimum Total Drag

This section compares the waveriders that are optimized for maximum L/D with those optimized for minimum total drag. Maximizing for L/D can be thought of as searching for the most efficient hypersonic cruising configuration, while minimizing C_D corresponds to finding the best accelerator type hypersonic vehicle. Figure 19 compares the configurations of two cone flow derived waveriders at Mach 6 for these two types of optimization. The same comparison is made for waveriders designed from flow over a 3/4 power-law body, at a Mach number of 14, in Figure 20. It is evident that optimizing for maximum L/D and minimizing for total drag lead to quite different waverider configurations. For the cone-flow Mach 6 case shown in Figure 19, the value of L/D is 7.175 when maximizing L/D and 7.187 when minimizing drag. The value of the drag coefficient, C_D, for the drag minimization case (C_D = 0.004222) is lower than for the case of maximizing L/D (C_D = 0.004694). The corresponding numbers for the Mach 14, power-law body case are L/D equal to 6.484 and C_D of 0.003095 for the maximization of L/D and L/D equal to 6.533 and CD of 0.003033 for the total drag minimization. These are the usual trends seen in the data for all of the cases run.

D. Study Concerning the Nature of the Boundary Layer

A study was made to determine the effect of using an all laminar, an all turbulent, and a transiting boundary layer in the design of an optimized waverider. Figure 21 shows representative results for optimization using flow over a 1/2 power-law body at a Mach number of 6. The figure shows perspective views of the resulting waveriders when the different types of boundary layers are assumed. The value of L/D is 9.97 for the all laminar case, 7.35 for the all turbulent case, and 7.46 for the transisting case. The low value of L/D for the transisting flow suggests that much of the waverider surface is covered with turbulent flow. The data for this case confirms this conclusion, indicating an early transition from laminar to turbulent flow.

E. Computing Time

As stated earlier, 100 optimization levels or iterations are used in the optimization of a waverider configuration. This requires approximately 5 to 15 minutes of CPU time on a UNIVAC 1190 computer, depending on the type of flow field generating body used. The short running time of the waverider optimization program makes it possible to conduct parametric studies with these class of vehicles.

IV. CONCLUSIONS

The following conclusions are made from the present waverider optimization study:

1. The present results are the first examples of viscous optimizated waveriders designed from axisymmetric flow fields, such as the hypersonic flow fields over minimum drag bodies.

2. The waveriders designed from flow fields over power-law bodies show promise, in terms of high L/D and minimum drag, when compared with conical-flow waveriders or other hypersonic configurations.

3. Optimization for a hypersonic cruise aircraft (maximizing L/D) results in a distinctly different configuration than optimization for a hypersonic accelerator aircraft (minimizing C_D).

4. The transition model used in the present study results in turbulent flow over much of the waverider surface. The nature of the boundary layer has a large effect on the aerodynamic characteristics of the vehicle. Better prediction methods for transition in hypersonic flows is badly needed.

V. ACKNOWLEDGEMENT

This work has been supported by the Minta Martin Aeronautical Fund of the University of Maryland. Also in support of this work, the authors have enjoyed a close working relationship with the McDonnell Douglas Aircraft Company and the Supersonic/Hypersonic Branch at the NASA Langley Research Center.

REFERENCES

1. Anderson, John D., Jr., "A Survey of Modern Research in Hypersonics," AIAA Paper 84-1578, invited paper given at the AIAA 17th Fluid Dynamics, Plasma Dynamics, and Lasers Conference, Snowmass, Colorado, June 25-27, 1984.

2. Bowcutt, Kevin G., Anderson, John D., Jr., and Capriotti, D.P., "Viscous Optimized Hypersonic Waveriders," AIAA Paper 87-0272, presented at the AIAA 25th Aerospace Sciences Meeting, Reno, Nevada, January 12-15, 1987.

3. Bowcutt, K.G., Anderson, J.D., Jr., and Capriotti, D.P., "Numerical Optimization of Conical Flow Waveriders Including Detailed Viscous Effects," in Aerodynamics of Hypersonic Lifting VEhicles, AGARD-CPP-428, March 1987, pp. 27/1-27/23.

4. Wallace Sawyer and Patrick Johnston, NASA Langley Research Center, private communication, 1985.

5. Bowcutt, Kevin G., Optimization of Hypersonic Waveriders Derived from Cone Flows--Including Viscous Effects, Ph.D. Dissertation, Department of Aerospace Engineering, University of Maryland, College Park, Maryland, 1986.

6. Corda, Stephen, Ph.D. Dissertation, Department of Aerospace Engineering, University of Maryland, College Park, Maryland, to be completed December 1987.

7. Nonweiler, T.R.F., "Aerodynamic Problems of Manned Space Vehicles," Journal of the Royal Aeronautical Society, Vol. 63, 1959, pp. 521-528.

8. Seddon, J. and Spence, A., "The Use of Known Flow Fields as an Approach to the Design of High Speed Aircraft," in Hypersonic Boundary Layers and Flow Fields, AGARD CP No. 30, May 1968, pp. 10/1-10/21.

9. Towend, L.H., "Research and Design for Lifting Reentry," Progress in Aerospace Sciences, Vol. 18, 1979, pp. 1-80.

10. Jones, J.G., Moore, K.C., Pike, J., and Roe, P.L., "A Method for Designing Lifting Configurations for High Supersonic Speeds, Using Axisymmetric Flow Fields," Ingenieur-Archiv, Vol. 37, pp. 56-72.

11. Rasmussen, M.L., "Waverrider Configurations Derived from Inclined Circular and Elliptic Cones," J. of Spacecraft and Rockets, Vol. 17, No. 6, Nov.-Dec. 1980, pp. 537-545.

12. Rasmussen, M.L., and Clement, L.W., "Cone-Derived Waveriders with Longitudinal Curvature," AIAA Paper No. 84-2100, 1984.

13. Cole, J.D., and Zien, T.F., "A Class of Three-Dimensional Optimum Hypersonic Wings," AIAA Journal, Vol. 7, No. 2, Feb. 1969, pp. 264-271.

14. Kim, B.S., Rasmussen, M.L., and Jischke, M.C., "Otimization of Waverider Configurations Generated from Axisymmetric Conical Flows," AIAA Paper 82-1299, 1982.

15. Nelder, J.A., Mead, R., "A Simplex Method for Function Minimzation", Computer Journal, Vol. 7, Jan. 1965, pp. 308-313.

16. Zucrow, M.J., and Hoffman, J.D., Gas Dynamics, John Wiley and Sons, New York, 1972.

17. Anderson, John D., Jr., Modern Compressible Flow with Historical Perspective, McGraw-Hill Book Co., New York, 1982.

18. Eckert, E.R.G., "Engineering Relations for Heat Transer and Friction in High-Velocity Laminar and Turbulent Boundary-Layer Flow Over Surfaces With Constant Pressure and Temperature," Transactions of the ASME, Vol. 78, No. 6, August 1956.

19. DiCristina, V., "Three-Dimensional Laminar Boundary Transition on a Sharp 8 Degree Cone at Mach 10", AIAA Journal, Vol. 8, No. 5, May 1970, p. 855.

20. Van Wie, D.M., An Application of Computational Fluid Dynamics to the Design of Optimum Ramjet and Powered Missile Components, Ph.D. Dissertation, Department of Aerospace Engineering, University of Maryland, College Park, Maryland, 1985.

21. Fetterman, D.E., "Favorable Interference Effects on Maximum Lift-Drag Ratios on Half-Cone Delta-Wing Configurations at Mach 6.86," NASA TN D-2942, August 1965.

TABLE 1

Experimental and Numerical Calculations of the Hypersonic Flow over a Cone-Wing

$M_\infty = 6.86$, $Re_L = 1.43 \times 10^6$, $L = 6.404$ in.

$\theta_{cone} = 4°$, $\Lambda_{delta} = 81°$, $T_\infty = 59.2$ K, $T_o = 617$ K

Case	T_{wall}(K)	C_L	C_D	L/D
experiment	?	.012	.0045	2.67
numerical (freestream upper surface)	59.2	.0126	.00329	3.83
	617.	.0126	.00294	4.29
numerical (1° compression upper surface)	59.2	.0126	.00198	1.05
	617.	.0126	.00115	1.10

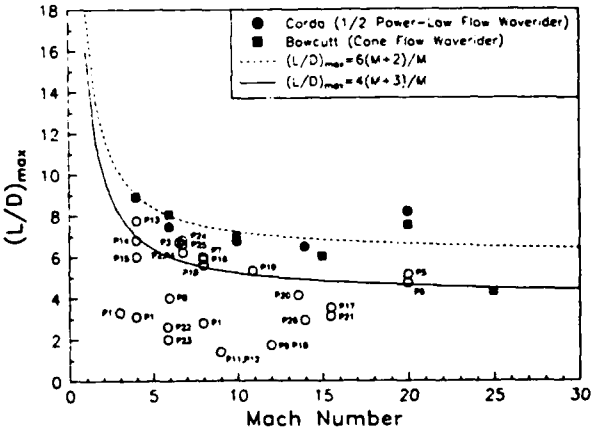

FIG. 1: Maximum lift-to-drag ratio comparison for various hypersonic configurations

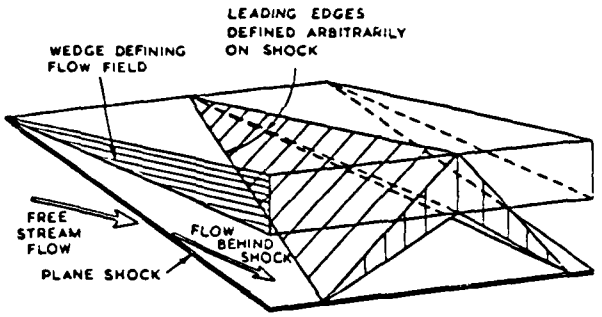

CONSTRUCTION FROM KNOWN FLOW FIELD

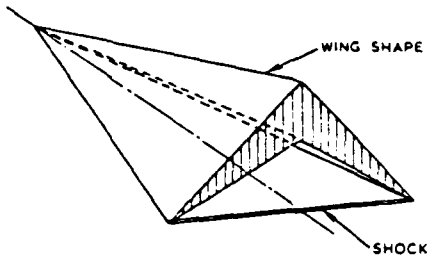

RESULTING WING AND SHOCK

FIG. 2: Nonweiler or caret wing (from Ref. 8)

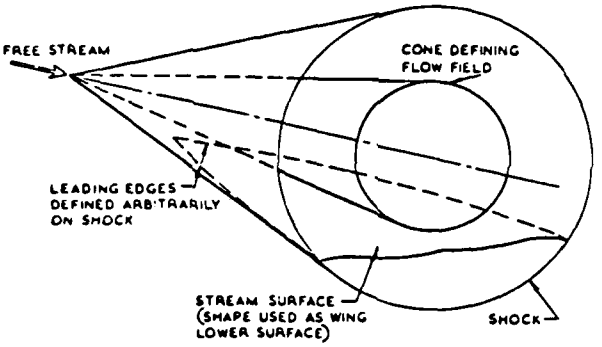

CONSTRUCTION FROM KNOWN FLOW FIELD

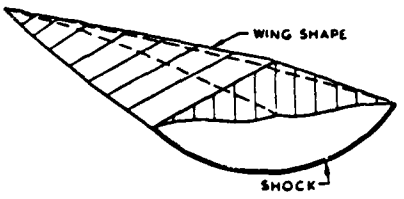

RESULTING WING AND SHOCK

FIG. 3: Cone-flow wing (from Ref. 8)

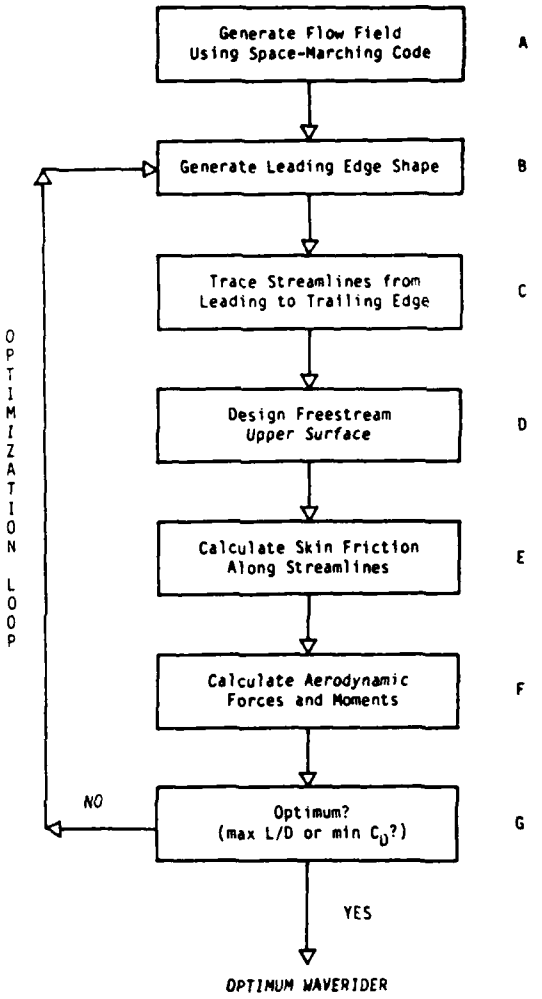

FIG. 4: Waverider design process

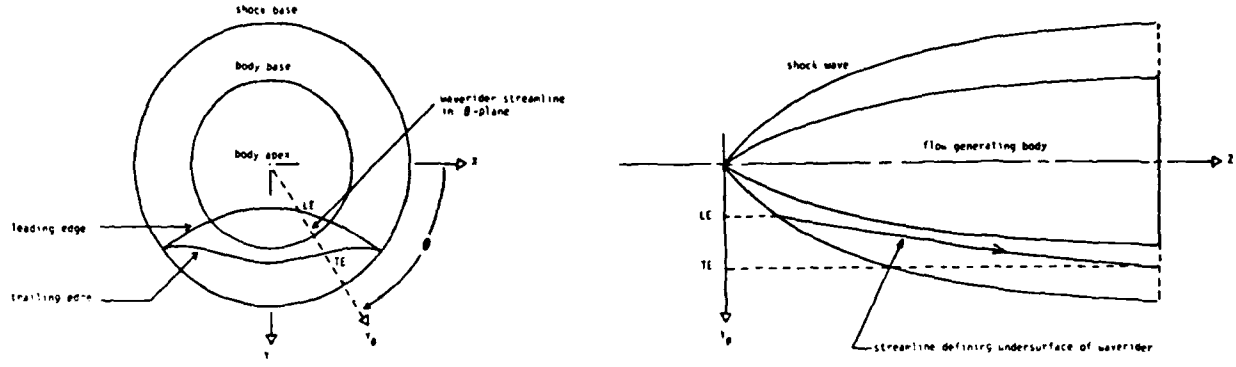

FIG. 5: Waverider construction

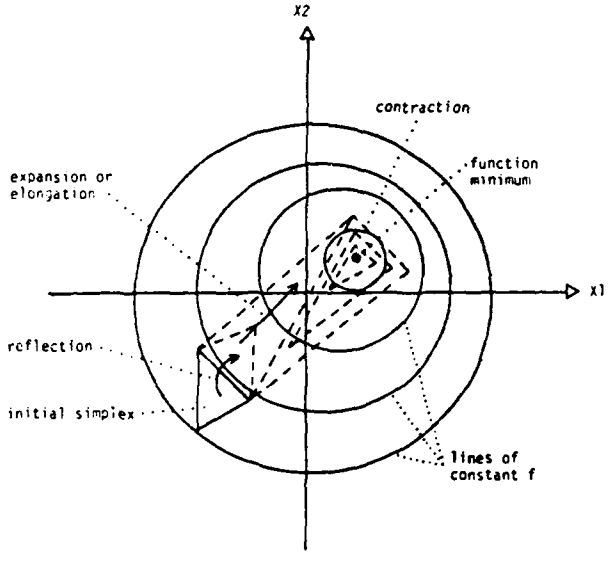

FIG. 6: Contour map example of simplex method for a function, f, of two variables

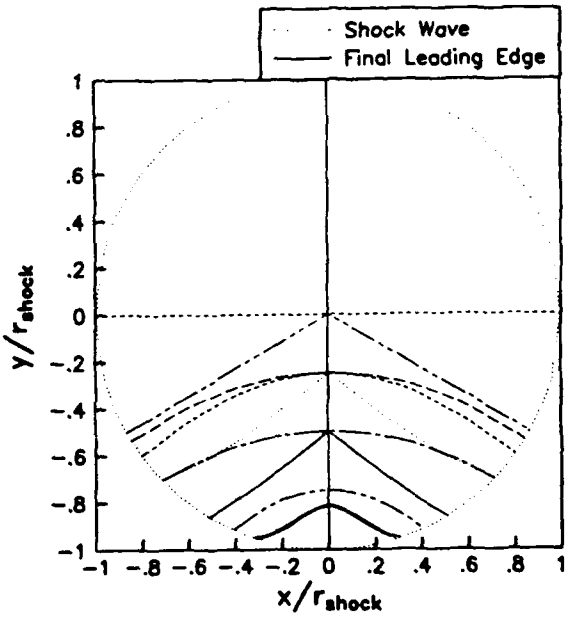

FIG. 7: Example of initial and optimized waverider design

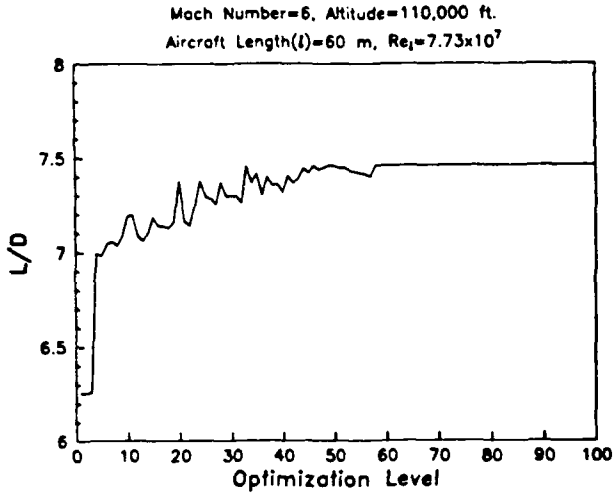

FIG. 8: Typical optimization history for waverider design

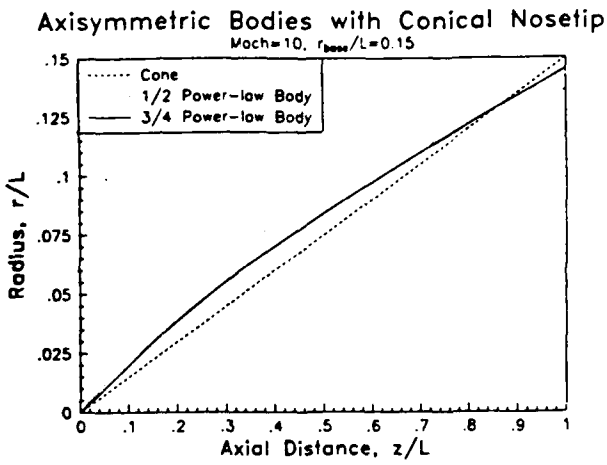

FIG. 9: Example of flow generating bodies

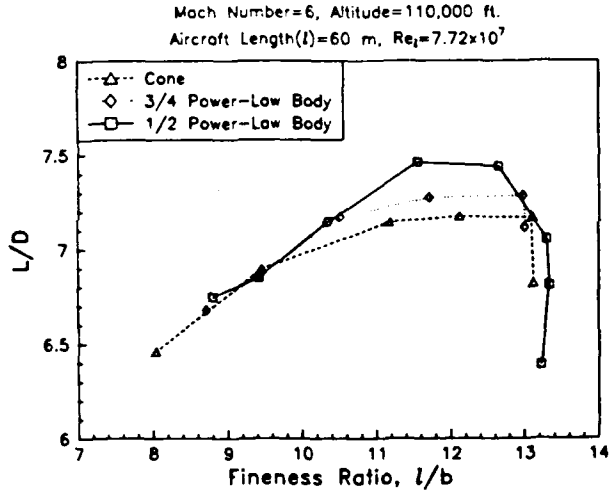

FIG. 10: Lift-to-drag ratio versus fineness ratio for a series of Mach 6 optimized waveriders

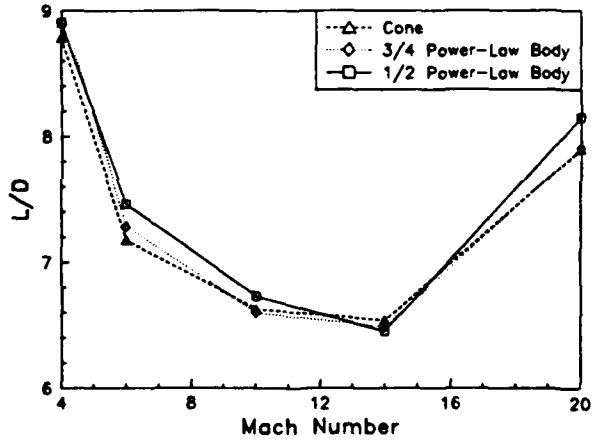

FIG. 11: Lift-to-drag ratio versus Mach number for the optimum waveriders

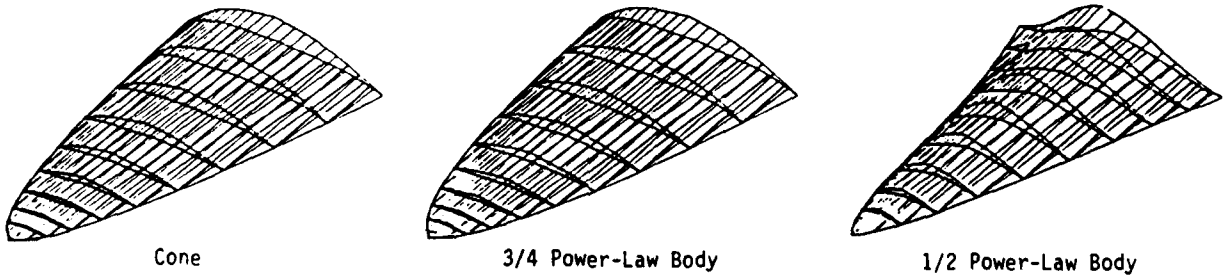

FIG. 12: Perspective views of Mach 6 optimum waveriders

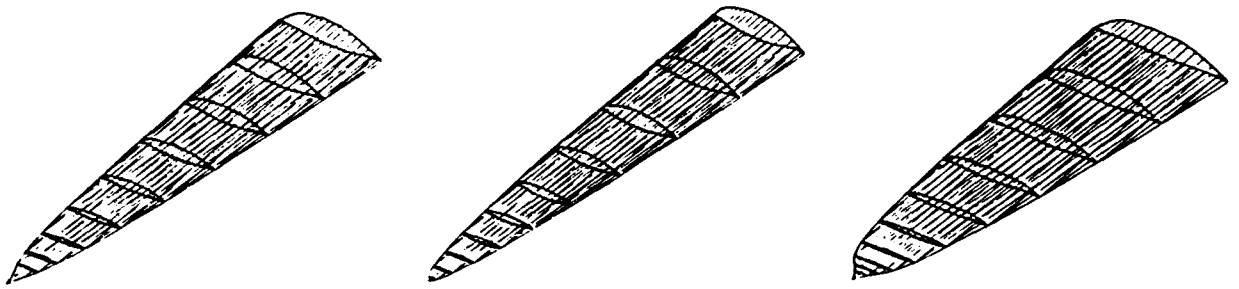

FIG. 13: Perspective views of Mach 20 optimum waveriders

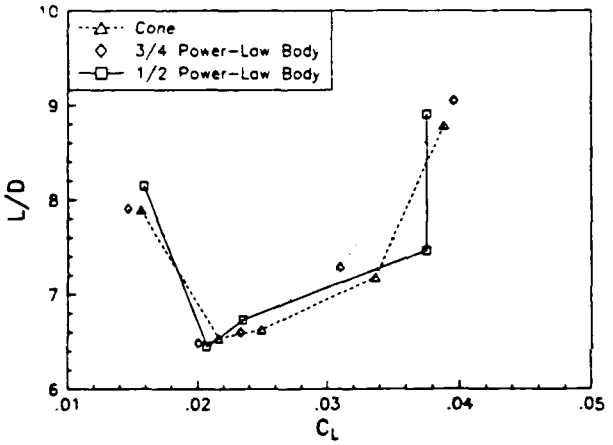

FIG. 14: Lift-to-drag ratio versus lift coefficent for the optimum waveriders

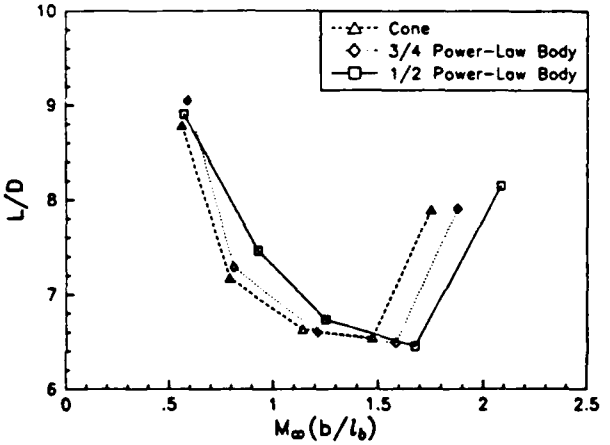

FIG. 15: Lift-to-drag ratio versus the hypersonic similarity parameter for the optimum waveriders

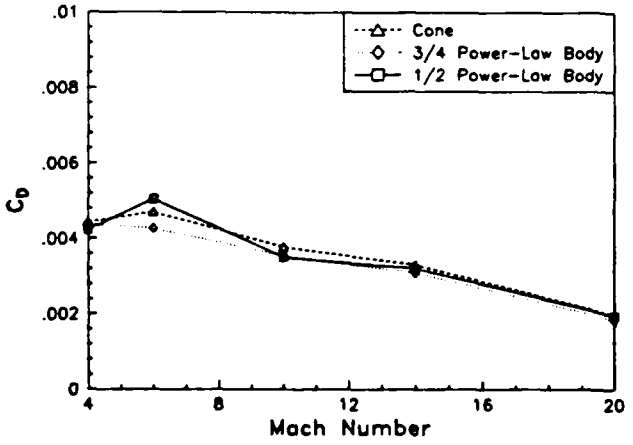

FIG. 16: Drag coefficient versus Mach number for the optimum waveriders

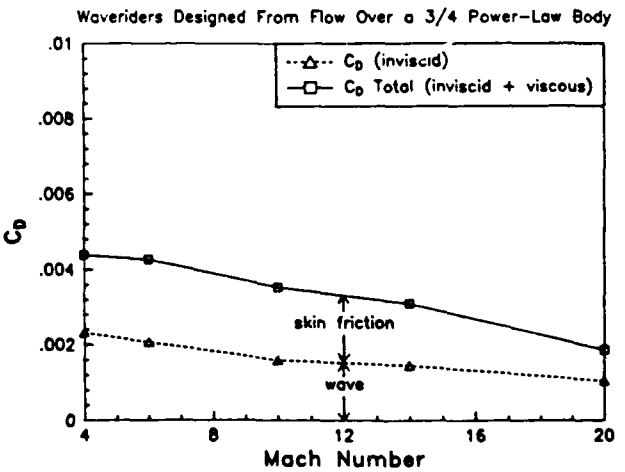

FIG. 17: Drag components for optimum waveriders designed from flow over a 3/4 power-law body

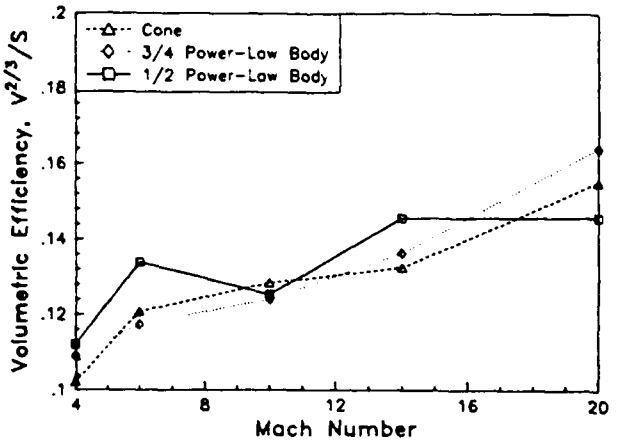

FIG. 18: Volumetric efficiency versus Mach number for the optimum waveriders

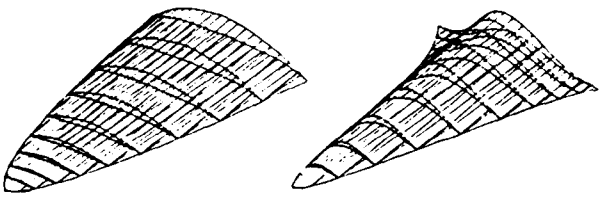

Max L/D Min C_D

FIG. 19: Perspective views of Mach 6 waveriders optimized for different figures of merit

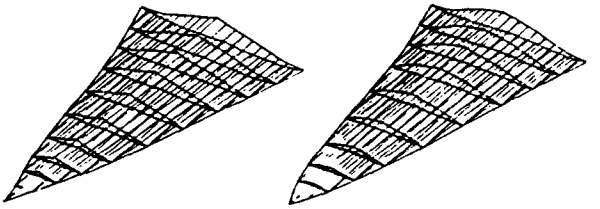

Max L/D Min C_D

FIG. 20: Perspective views of Mach 14 waveriders optimized for different figures of merit

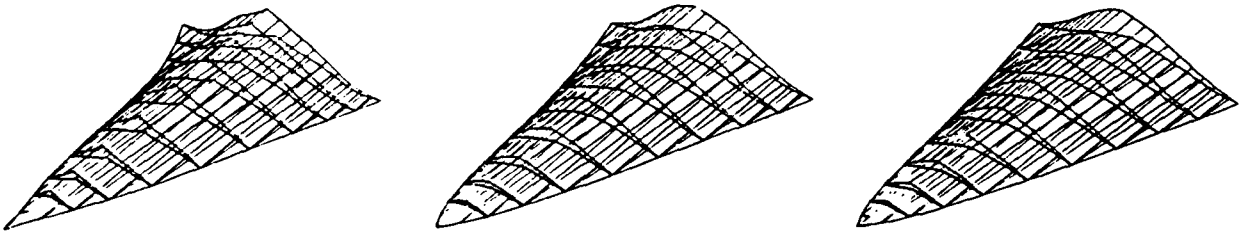

All Laminar Transisting All Turbulent

FIG. 21: Perspective views of optimized Mach 6 waveriders designed with different boundary layer characteristics

-- NOTES --

AIAA'87

AIAA-87-0272
Viscous Optimized Hypersonic Waveriders

K. G. Bowcutt, J. D. Anderson and D. Capriotti, Univ. of Maryland, College Park, MD

AIAA 25th Aerospace Sciences Meeting

January 12-15, 1987/Reno, Nevada

VISCOUS OPTIMIZED HYPERSONIC WAVERIDERS

by

Kevin G. Bowcutt,* John D. Anderson, Jr.,** and Diego Capriotti***

Department of Aerospace Engineering
University of Maryland
College Park, Maryland 20742

"It is really not foreseeable that an 'optimized' calculated shape could do anything more than give a guide to the designer. However, it is only a guide that the designer actually wants from the aerodynamicist. He would really be a little embarrassed to be offered a perfect aerodynamic shape, which he would then have to carve holes in, add fairings, and so on, in order to satisfy such mundane requirements as that the pilot should be able to see where he is going or that people have somewhere convenient to get in and out."

P.L. Roe
Royal Aircraft Establishment
January 1970

ABSTRACT

A family of optimized hypersonic waveriders is generated and studied wherein detailed viscous effects are included within the optimization process itself. This is in contrast to previous optimized waverider work, wherein purely inviscid flow is used to obtain the waverider shapes. For the present waveriders, the undersurface is a streamsurface of an inviscid conical flowfield, the upper surface is a streamsurface of the inviscid flow over a tapered cylinder (calculated by the axisymmetric method of characteristics), and the viscous effects are treated by integral solutions of the boundary layer equations. Transition from laminar to turbulent flow is included within the viscous calculations. The optimization is carried out using a non-linear simplex method. The resulting family of viscous hypersonic waveriders yields predicted high values of lift/drag, high enough to break the "L/D barrier" based on experience with other hypersonic configurations. Moreover, the numerical optimization process for the viscous waveriders results in distinctly different shapes compared to previous work with inviscid-designed waveriders. Also, the fine details of the viscous solution, such as how the shear stress is distributed over the surface, and the location of transition, are crucial to the details of the resulting waverider geometry.

I. INTRODUCTION

Over the past few years, interest in all aspects of hypersonic flight has grown explosively, driven by new vehicle concepts such as the National Aerospace Plane (NASP), aero-assisted orbital transfer vehicles (AOTV's), the hypersonic transport (the "Orient Express"), and hypersonic missiles, to name just a few. An extended discussion of these concepts, as well as a survey of hypersonic aerodynamic research contrasting the "old" with the "new" hypersonics, is given in Ref.1. Hence no further elaboration will be given here.

The present paper deals with a class of advanced hypersonic lifting configurations. To help understand the motivation for the present work, the following background is given. For a lifting aerodynamic body, it is well-known that high maximum lift-to-drag ratios, $(L/D)_{max}$, are very difficult to obtain at hypersonic speeds, due to the presence of strong shock waves (hence high wave drag) and massive viscous effects. At supersonic and hypersonic speeds, the most efficient lifting surface is the infinitely thin flat

* Graduate Hypersonic Aerodynamics Fellow, sponsored by the Army Research Office, Dr. Robert Singleton, monitor. Member, AIAA. Presently, Engineer, Rockwell International, Los Angeles.

** Professor. Fellow, AIAA. Currently on sabbatical as the Charles Lindbergh Professor at the National Air and Space Museum, Smithsonian Institution.

*** Graduate Research Assistant. Student member, AIAA.

plate; the inviscid hypersonic aerodynamic properties of a flat plate are shown as the solid curves in Fig.1, based on the Newtonian limit of free stream Mach number $M_\infty \to \infty$ and $\gamma = C_p/C_v \to 1$. Note that L/D theoretically approaches infinity as the angle-of-attack, α, approaches zero. In reality, viscous effects will cause L/D to peak at low values of α, and to go to zero as $\alpha \to 0$. This is illustrated by the dashed line in Fig.1, which shows the variation of L/D modified by skin friction as predicted by a reference temperature method described in Ref. 2. Although the infinitly thin flat plate shown in Fig.1 is the most effective lifting surface aerodynamically, it is the least effective in terms of volume capacity. It goes without saying that all practical flight vehicles must have a finite volume to carry fuel, payload, etc. Hence, the flat plate results, although instructive, are of academic interest only. In contrast, Fig. 2 shows values of $(L/D)_{max}$ versus the volume parameter $V^{2/3}/S$ for several generic hypersonic configurations, obtain-from Ref. 3. Here, V is the body volume and S is the planform area. Note from Fig.2 that typical hypersonic values of $(L/D)_{max}$ range from 4 to 6 for such lifting bodies at the conditions shown. These values are also typical of the hypersonic transport configuration studied in Ref. 4. Clearly, values of $(L/D)_{max}$ for hypersonic vehicles are substantially lower than those for conventional subsonic and low supersonic airplanes. (For example, the maximum L/D values for the World War II Boeing B-29 and the contemporary General Dynamics F-111 are 16.8 and 15.8 respectively, as obtained from Ref. 5). Indeed, as M_∞ increases across the supersonic and hypersonic regimes, there is a general empirical correlation for $(L/D)_{max}$ based on actual flight vehicle experience, given by Kuchemann[6]:

$$(L/D)_{max} = \frac{4(M_\infty + 3)}{M_\infty}$$

This variation is shown as the solid curve in Fig.3. Also shown are a number of data points for various previous hypersonic vehicle configurations at various Reynolds numbers (the open symbols), as well as new results from the present investigation (the solid symbols). Fig. 3 is pivotal to the present paper, and will be discussed at length in subsequent sections. However, at this stage in our discussion, Fig.3 is used to illustrate only the following aspects:

1. The solid curve represents a type of "L/D barrier" for conventional hypersonic vehicles, which is difficult to break.
2. Data for conventional hypersonic vehicles, shown as the open circles, form an almost random "shotgun" pattern which, for the most part, falls below the solid curve.
   (The numbers adjacent to these open circles pertain to specific reference numbers itemized in Ref. 7, which should be consulted for details.)
3. The solid symbols pertain to the present study, and represent a new class of hypersonic configurations which break the "L/D barrier." These configurations are conical flow waveriders that are optimized with detailed viscous effects included directly in the optimization process.

To help understand the contribution made by the present work, let us briefly review the general concept of waveriders. In 1959, the design of three-dimensional hypersonic vehicles which support planar attached shock waves was introduced by Nonweiller,[8,9] who hypothesized that streamsurfaces from the flow behind a planar oblique shock could be used as supersonic lifting surfaces. This led to a class of vehicles with a caret-shaped transverse cross-section and a delta planform-- the so-called caret wing as shown in Fig.4. Here, the body surface is generated by stream surfaces behind a planar oblique shock wave. The shock wave is attached to the sharp leading edges at the design Mach number, and hence no flow spillage takes place around the leading edge. The lift is high due to the high pressures behind a two-dimensional planar shock wave, exerted on the lower surface of the vehicle. Because the body appears to be riding on top of the attached shock wave, it is called a "waverider". The aerodynamic advantages of such waveriders are listed in Ref. 1, and are discussed in great detail in Refs. 7 and 10. In short, without repeating the details here, at a given lift coefficient, caret waveriders theoretically operate at higher L/D values than other hypersonic configurations.

Expanding on this philosophy, other types of flowfields can be used to generate waveriders. For example, any streamsurface from the supersonic flow over an axisymmetric body can be used to generate a waverider with an attached shock wave along its complete leading edge. Work on such waveriders was first carried out in Britain, as nicely summarized in Ref. 11, where the flow over a right-circular cone at zero degrees angle of attack is used to generate a class of "conical flow" waveriders. Still later, waveriders were generated from inclined circular and elliptic cones, and axisymmetric bodies with longitudinal curvature by Rasmussen et al.[12,13], using hypersonic small disturbance theory. This work was further embelished by the search for optimized waverider shapes. For example Cole and Zien[14] found optimized waveriders derived from axisymmetric bodies with longitudinal curvature by using hypersonic small disturbance theory to generate inviscid flow solutions, and then utilizing the calculus of variations to obtain the optimum waverider shapes. Later, Kim et al. used the same philosophy to derive optimum waveriders from flowfields about unyawed circular cones[15], and yawed circular and elliptic cones[16]. In Refs. 14-16, the advantage of hypersonic small disturbance theory is that analytic expressions are obtained for surface pressure distributions, hence lift and wave drag, thus enabling the application of the calculus of variations for optimization.

Unfortunately, to date the potential superiority of waveriders as hypersonic high L/D shapes has not been fully demonstrated, either in the wind tunnel or in flight. A basic problem arises because of the tendency for waveriders to have large wetted surface areas, which leads to large friction drag. All previous waverider optimization work (such as Refs. 14-16) has been based on the assumption of inviscid flow, after which an estimate of skin friction for the resulting configuration is sometimes added. As a result, the real aerodynamic performance of the resulting optimum configuration usually falls short of its expectations.

The purpose of the present work is to remove this deficiency. In particular, a series of conical-flow generated waveriders are optimized for maximum L/D wherein detailed viscous effects (including boundary layer transition) are included within the optimization process itself. This leads to a new class of waveriders where the optimization process is trying to reduce the wetted surface area, hence reducing skin friction drag, while at the same time maximizing L/D. Because detailed viscous effects can not be couched in simple analytical forms, the formal optimization methods based on the calculus of variations can not be used. Instead, in the present work a numerical optimization technique is used, based on the simplex method by Nelder and Mead[17]. By using a numerical optimization technique, other real configuration aspects can be included in the analysis in addition to viscous effects, such as blunted leading edges, and an expansion upper surface (in contrast to the standard assumption of a free stream upper surface, i.e., an upper surface with all generators parallel to the freestream direction). The results of the present study lead to a new class of waveriders, namely "viscous optimized" waveriders. Moreover, these waveriders appear to produce relatively high values of (L/D), as will be discussed in subsequent sections.

II. ANALYSIS

For the present waverider configurations, the following philosophy is followed:

1. The lower (compression) surface is generated by a streamsurface behind a conical shock wave. The inviscid conical flowfield is obtained from the numerical solution of the Taylor-Maccoll equation, derived for example in Ref. 18.

2. The upper surface is treated as an expansion surface, generated in a similar manner from the inviscid flow about a tapered, axisymmetric cylinder at zero angle of attack, and calculated by means of the axisymmetric method of characteristics.

3. The viscous effects are calculated by means of an integral boundary layer analysis following surface streamlines, including transition from laminar to turbulent flow.

4. Blunt leading edges are included to the extent of determining the maximum leading edge radius required to yield acceptable leading edge surface temperatures, and then estimating the leading edge drag by modified Newtonian theory.

5. The final waverider configuration, optimized for maximum L/D at a given Mach number and Reynolds number with body fineness ratio as a constraint, is obtained from the numerical simplex method taking into account all the effects itemized in 1-4 above within the optimization process itself.

The following paragraphs describe each of the above items in more depth; for a highly detailed discussion, see Ref. 7.

A. Inviscid Flow -- Lower Surface

The waverider's lower surface is generated from a streamsurface behind a conical shock wave supported by a hypothetical right circular cone at zero angle of attack. The hypothetical cone and its flowfield is shown in Fig. 5, where θ_c is the cone semi-angle and θ_s is the wave angle. The inviscid conical flow is obtained from the Taylor-Maccoll equation[18]

$$\frac{\gamma-1}{2}\left[1-V_r^2-\left(\frac{dV_r}{d\theta}\right)^2\right]\left[2V_r+\frac{dV_r}{d\theta}\cot\theta+\frac{d^2V_r}{d\theta^2}\right] - \frac{dV_r}{d\theta}\left[V_r'\frac{dV_r}{d\theta}+\frac{dV_r}{d\theta}\frac{d^2V_r}{d\theta^2}\right] = 0 \qquad (1)$$

solved by a standard Runge-Kutta, forth-order accurate numerical technique, namely the RKF45 algorithm obtained from Ref. 19. In Eq.(1), V_r is the component of nondimensional flow velocity along a conical ray, θ is the angle of the ray referred to the cone axis, and γ is the ratio of specific heats.

Any streamsurface from this flowfield can represent the wing undersurface of a waverider, as shown in Fig. 6. (For purposes of illustration, Fig. 6 also shows the waverider upper surface as a freestream surface, but this is only one of many possible choices for the upper surface.) Any particular undersurface is uniquely defined by the intersection of the conical flow streamsurface with the conical shock wave, as shown by the curve labeled "leading edge" in Fig. 7. Let us examine Fig.7 more closely. It is a front-view of the hypothetical conical flowfield, illustrating the cone apex at the center, and both the cone base and shock base at some arbitrary distance downstream of the apex. Consider a curve in this front-view, lying below the apex (or even including the apex), as shown by the curve labeled "leading edge". Now construe this curve as a trace on the conical shock wave itself, and visualize streamlines trailing downstream from this trace; the resulting streamsurface is the waverider undersurface sketched in Fig. 6. Indeed, the curve labeled "leading edge" in Fig. 7 is simply the forward projection of the waverider leading edge on the cross-flow (x-y) plane. This curve is treated as completely general, except for the constraints that it be symmetric about the y-z plane, and that it lie entirely below the x-z plane to ensure that the waverider undersurface is a compression surface. Also in Fig. 7, note the curve labeled "trailing edge". This is the intersection of the particular conical flow streamsurface with the plane of the shock base, and it represents the bottom surface trailing edge of the waverider. This is the shape of the bottom of the waverider base, as sketched in Fig. 6. Returning to Fig.7, the area between the "leading edge" and "trailing edge" curves is the forward projection of the entire waverider compression surface. Moreover, the dashed line emanating from the cone apex in Fig. 7 is the forward projection of a conical flow streamline; hence, that portion of the dashed line contained between the "leading edge" and "trailing edge" curves is the projection of a particular streamline along the waverider undersurface, from the leading edge to the trailing edge.

B. Inviscid Flow -- Upper Surface

In most previous waverider work, the upper surface is treated as a freestream surface, as illustrated in Fig. 6. Here, the upper surface pressure is freestream pressure, p_∞. However, if the upper surface is made an expansion surface, where $p<p_\infty$, then a small but meaningful contribution to L/D can be obtained. This approach is taken here. Similar to the philosophy for the lower surface, the upper surface is a streamsurface "carved" from a known expansion flow. The hypothetical expansion body chosen here is a circular cylinder of given radius; the cyclinder is aligned parallel to the flow and, at some point, is tapered parabolically to a smaller radius. The result is an axisymmetric expansion flow, where the domain of expansion is bounded by a freestream Mach cone centered on the cy linder axis, as shown in Fig. 8. Parabolic taper was chosen because it is relatively simple, and the resulting expansion body slope is everywhere continuous. Once the expansion body is chosen, it remains only to geometrically position the expansion region relative to the lower surface, choose the initial and final cylinder radii, solve the inviscid expansion flow, then cut a streamsurface from that flow to serve as the waverider upper surface. This basic idea was first developed for two-dimensional expansions by Flower[20], and later for axisymmetric expansions by Moore[21].

The axisymmetric flow is calculated from the axisymmetric method of characteristics, using the two-step predictor-corrector iteration scheme of Ferri[22]. The details involving the matching of the resulting expansion surface with the conical flow compression surface are straight forward, but lengthy. Considering that the expansion surface contributes only about 10% to the value of (L/D), no further space for its discussion is justified in the present paper; for the complete discussion, see Ref. 7.

C. Leading-Edge Bluntness

Waveriders, by design, have sharp leading edges that support attached shock waves. However, for flight Mach numbers above five, the temperatures for sharp leading edges will exceed the practical limits of most structural materials. This leads to the need for blunt leading edges with sufficiently large radii such that the aerodynamic heat flux is reduced to reasonable levels. However, at the same time the leading edge radius should be as small as possible to reduce the nose drag.

To reduce the required leading edge radius, Nonweiler[23] has proposed adding conducting material aft of the leading edge to transport thermal energy away from the region of high convective heating near the stagnation or attachment line, and conduct it downstream to areas where convective heating is lower, and excess energy can be radiated away from the body. Nonweiler labeled this theoretical concept as a "conducting plate", which is somewhat analogous to other passive cooling techniques, such as heat pipes. Using Nonweiler's basic technique, minimum leading edge radii can be ascertained, once flight Mach number, freestream conditions, leading edge sweep, material properties, and maximum allowable temperature are known.

In the present work, Nonweiler's technique was used to determine the leading edge radii for waveriders designed for Mach numbers between 6 and 25. The leading edge material used for the calculations was ATJ graphite, chosen because it is representative of materials with high conductivity and high melting point temperature. Details of this technique as applied to the present work are given in Ref. 7. It is interesting to note that, for conditions associated with the typical flight path of a lifting hypersonic vehicle entering the earth's atmosphere at Mach 25 and decelerating to Mach 6 at lower altitude, the minimum leading edge diameters ranged from 6 to 28 mm -- quite small in comparison to a typical overall length of, say 60m. Therefore, the present waveriders are essentially "aerodynamically sharp" from that point of view. Regardless of the apparently small amount of required leading edge bluntness (from the aerodynamic heating point of view), the present waveriders were geometrically altered to accomodate the blunt edge, and the contribution to aerodynamic forces on the waverider were estimated assuming a modified Newtonian pressure distribution on the leading edge.

D. Viscous Flow Analysis

A major aspect of the present investigation is that optimum waverider shapes are obtained wherein detailed viscous effects are included within the optimization process itself. These viscous effects are calculated by means of two integral boundary layer techniques, described below. In all cases, the boundary layer flow is assumed to be locally two-dimensional, following the inviscid upper surface and lower surface streamlines. Both laminar and turbulent flow are considered, along with a transition region based on empirical correlations.

D.1 Laminar Analysis

The laminar boundary layer calculations were performed using Walz' integral method, as described in Ref. 24. The method requires the solution of a set of coupled first-order ordinary differential equations along the boundary layer edge streamlines. These equations are the boundary layer momentum and mechanical energy equations, given by

Momentum:
$$Z' + \frac{u_e'}{u_e} F_1 Z - F_2 = 0 \qquad (2)$$

Mechanical Energy:
$$W' + \frac{u_e'}{u_e} F_3 W - \frac{F_4}{Z} = 0 \qquad (3)$$

where

$$Z = \delta_2 \left(\frac{\rho_e u_e \delta_2}{u_w}\right) \qquad (4)$$

$$W = \delta_3/\delta_2 \qquad (5)$$

$$\delta_1 \equiv \int_0^\delta \left(1 - \frac{\rho u}{\rho_e u_e}\right) dy \qquad (6)$$

$$\delta_2 \equiv \int_0^\delta \frac{\rho u}{\rho_e u_e}\left(1 - \frac{u}{u_e}\right) dy \qquad (7)$$

$$\delta_3 \equiv \int_0^{\delta} \frac{\rho u}{\rho_e u_e}\left(1 - \frac{u^2}{u_e^2}\right)dy \qquad (8)$$

and

$$F_1 = 3+2H-M_e^2+n\,\frac{u_w'/u_w}{u'/u_e}\,,\quad n = \begin{cases}0, & T_w = \text{constant}\\ 1, & T_w \neq \text{constant}\end{cases} \qquad (9)$$

$$F_2 = 2a/b \qquad (10)$$

$$F_3 = 1-H+r(\gamma-1)M_e^2\left(1-\frac{\tilde{\theta}}{W}\right) \qquad (11)$$

$$F_4 = (2\beta-aW)/b \qquad (12)$$

Note that in the above equations, primes denote differentiation with respect to x, here representing the boundary layer coordinate in the streamline direction. The variables in Eqs. (9)-(12) are defined by Walz to be

$$H = \delta_1/\delta_2 = bH_{12}+r\,\frac{\gamma-1}{2}\,M_e^2(W-\tilde{\theta}) \qquad (13)$$

$$a = 1.7261\ (W^*-1.515)^{0.7158} \qquad (14)$$

$$b = \frac{(\delta_2)_u}{\delta_2} = 1+r\,\frac{\gamma-1}{2}\,M_e^2(W-\tilde{\theta})(2-W) \qquad (15)$$

$$r = \sqrt{Pr} \qquad (16)$$

$$\tilde{\theta} = \frac{T_{aw}(x)-T_w(x)}{T_{aw}(x)-T_e(x)} \qquad (17)$$

and $$\beta = \beta_u x \qquad (18)$$

where

$$H_{12} = 4.0306 - 4.2845\ (W^*-1.515)^{0.3886} \qquad (19)$$

$$T_{aw} = T_e + \frac{ru_e^2}{2C_p} \qquad (20)$$

$$W^* = (\delta_3)_u/(\delta_2)_u = W/\psi \qquad (21)$$

$$\psi = 1 + \frac{(\psi_{12}-1)M_e}{M_e + \dfrac{\psi_{12}-1}{\psi_o'}} \qquad (22)$$

$$\psi_{12} = \frac{2-(\delta_1)_u/\delta}{W^*}\,\tilde{\theta} + \frac{1-(\delta_1)_u/\delta}{W^*g}\,(1-\tilde{\theta}) \qquad (23)$$

$$\psi_o' = 0.0144(2-W^*)(2-\theta)^{0.8} \qquad (24)$$

$$(\delta_1)_u/\delta = 0.420 - (W^*-1.515)^{0.424W^*} \qquad (25)$$

$$g = 0.324+0.336(W^*-1.515)^{0.555} \qquad (26)$$

$$\beta_u = 0.1564 + 2.1921\ (W^*-1.515)^{1.70} \qquad (27)$$

and

$$x = \left\{1+r\left(\frac{\gamma-1}{2}\right)M_e^2\left[1.16W^*-1.072-\tilde{\theta}(2W^*-2.581)\right]\right\}^{0.7} \cdot \left[1+r\left(\frac{\gamma-1}{2}\right)M_e^2(1-\tilde{\theta})\right]^{-0.7} \qquad (28)$$

Careful inspection of Eq. (21) reveals that it is an implicit equation for W*, since ψ is a complex function of W*. Therefore, in practice, a numerical zero-finding routine is used on Eq. (21) to find the value of W* that yields the known value of W. Walz suggested an approximation that would allow closed form solution of Eq. (21), however, the present authors have found that it made boundary layer calculations blow up when used for a Mach six flat plate test case. Hence, the suggested approximation was discarded in favor of the zero-finding approach. For more details on the numerical solution of these integral boundary layer equations, see Ref. 7.

D.2 Turbulent Analysis

If and when boundary layer transition is predicted, turbulent boundary layer calculations are performed using the inner variable integral method of White and Christoph[25]. In practice, the method requires solution of one of two first-order ordinary differential equations along the boundary layer edge streamlines, depending upon the value of the parameter λ/λ_{max}, where

$$\lambda = \sqrt{\frac{2}{C_f}} \qquad (29)$$

$$\lambda_{max} = 8.75\ \log_{10} Re^* \qquad (30)$$

$$S = \frac{(T_{aw}/T_e-1)^{1/2}}{\sin^{-1}A+\sin^{-1}B} \qquad (31)$$

and $$Re^* = \frac{\rho_e}{\mu_w}\left(\frac{T_e}{T_w}\right)^{1/2}\frac{u_e^2}{u_e'} \qquad (32)$$

In Eq. (31), the parameters A and B are defined as

$$A = a/c \qquad (33)$$

$$B = b/c \qquad (34)$$

where

$$a = \frac{T_{aw}+T_w}{T_e} - 2 \qquad (35)$$

$$b = \frac{T_{aw}-T_w}{T_e} \qquad (36)$$

$$c = \left[\left(\frac{T_{aw}+T_w}{T_e}\right)^2 - 4\,\frac{T_w}{T_e}\right]^{1/2} \qquad (37)$$

and Taw is defined by Eq. (20), except that now the recovery factor is the turbulent value,

$$r = Pr^{1/3} \qquad (38)$$

According to Ref. 24, if $\lambda/\lambda_{max} < 0.36$, or $Re^* < 0$, then the differential equation

$$\lambda' = \frac{1}{8}\frac{\rho_e}{\mu_w}\left(\frac{T_e}{T_w}\right)^{1/2} u_e \exp(-0.48\frac{\lambda}{S}) - 5.5\frac{u_e'}{u_e} \quad (39)$$

is valid; however if $\lambda/\lambda_{max} > 0.36$, then the equation

$$\lambda' = \frac{\frac{-u_e'}{u_e}(1+9S^{-2}g^*Re^{*0.07})}{0.16f^*S^3} + \frac{\left(\frac{u_e u_e'' - 2(u_e')^2}{u_e u_e'}\right)(3S^2 g^* Re^{*0.07})}{0.16f^*S^3} \quad (40)$$

applies, where

$$f^* = (2.434z + 1.443z^2)\exp(-44\ z^5) \quad (41)$$

$$g^* = 1 - 2.3z + 1.76z^3 \quad (42)$$

$$z = 1 - \lambda/\lambda_{max} \quad (43)$$

and the primes denote, as in the laminar case, differentiation with respect to the streamline coordinate, x. For more details concerning the numerical solution of these equations, see again Ref. 7.

D. 3 Transition Analysis

The prediction of transition from laminar to turbulent flow at hypersonic speeds is a state-of-the-art research topic. In the present analysis, the correlation used for predicting the onset of transition is based on two sets of data: (1) data for sharp cones at zero angle-of-attack[26]; and (2) data for wings with blunt, swept supersonic leading edges[27]. The correlation gives local transition Reynolds number Re_{x_t}, as a function of local edge Mach number, M_e, as follows[26]:

$$\log_{10}(Re_{x_t}) = 6.421\exp(1.209\times10^{-4}M_e^{2.641}) \quad (44)$$

In turn, this value of transition Reynolds number is modified for wing leading-edge sweep, as follows[27]:

$$\frac{(Re_{x_t})_\Lambda}{(Re_{x_t})_{\Lambda=0}} = 0.787\cos^{4.346}\Lambda - 0.7221e^{-0.0991\Lambda} + 0.9464 \quad (45)$$

where Λ is the sweep angle, and $(Re_{x_t})_{\Lambda=0}$ is obtained from Eq.(44).

Once the onset of transition has been predicted, the extent of the transition region, hence the end of transition, is predicted using a relationship developed by Harris and Blanchard[28], as follows:

$$x_{te} = x_{ti}[1+5(Re_x)_{ti}^{-0.2}] \quad (46)$$

where x_{te} and x_{ti} are the distances along a streamline from the leading edge to the beginning and end of transition, respectively, and $(Re_x)_{ti}$ the local Reynolds number at the beginning of transition obtained in the present analysis from Eq.(45).

The variation of local skin friction coefficient within the transitional region (between x_{te} and x_{ti}) is assumed to be a linear combination of the laminar (c_{f_L}) and turbulent (c_{f_T}) values that would have existed if the boundary layer were completely laminar or turbulent, respectively. The transitional friction coefficient, $c_{f_{TR}}$, is thus related to c_{f_L} and c_{f_T} by:

$$c_{f_{TR}} = (1-\xi)\ c_{f_L} + \xi\ c_{f_T} \quad (47)$$

where ξ is a weighting factor (a function of x) inspired by Emmons (as discussed in Ref.29). For the present investigation, the following expression for ξ is, as derived in detail in Ref. 7:

$$\xi(x) = 1 - e^{-3\{\exp[\frac{\ln 2}{5x_{ti}}(Re_x)_{ti}^{0.2}(x-x_{ti})]-1\}^2} \quad (48)$$

It is not possible within the current state-of-the-art to evaluate the accuracy of these transition correlations. After a study of the existing literature, the present authors feel that the above relations form a practical method for simulating transition within the goals of the present study. They provide a mechanism for assessing the effect of transition on optimum waverider shapes; indeed, as discussed in the results, one series of numerical experiments is conducted wherein the transition location is varied as a parameter.

E. Aerodynamic Forces

The lift, drag, and hence L/D is calculated from a detailed integration of the local surface pressures and shear stress over the waverider surface. Consistent with wind tunnel practice as well as other literature, base drag is not included in the present results. (For example, all the data shown in Fig. 3 do not include base drag.) This is done to enable a rational comparison with other data. Moreover, at very high Mach number, the base drag becomes a small quantity in comparison to forebody drag. Details on the pressure and shear stress numerical integration can be found in Ref. 7.

F. Waverider Optimization

Once a specific shape for the forward leading edge projection of a waverider is chosen, (such as shown in Fig. 7), the techniques outlined in the previous sections can be used to generate the corresponding waverider and evaluate its lift-to-drag ratio (L/D). Finding the leading edge shape that maximizes L/D, with all other parameters held fixed, then requires an optimization scheme that can systematically change the projected leading edge shape in search of the one that yields maximum L/D. Unfortunately, most existing optimization schemes require that the function of interest have an analytical description -- a requirement not possible in the present work. There is one scheme, however, a non-linear simplex method for function minimization by Nelder and Mead[31], that requires nothing more than the ability to numerically evaluate the

function. This scheme has been used in the present work to find optimum waveriders.

In general, the scheme of Ref.17 minimizes a function of n variables by comparing values of the function at (n+1) vertices of a "simplex", then replacing the vertex with the highest function value by another point determined via the logic of the scheme. As a result of the algorithm logic, "the simplex adapts itself to the local landscape [of the function surface], elongating down long inclined planes, changing direction on encountering a valley at an angle, and contracting in the neighborhood of a minimum", according to Ref.17. In this scheme, three operations -- reflection, contraction and expansion -- are used to modify the current simplex in an attempt to replace the vertex having the highest function value with one having a lower value. Each of three operations replace one or more of the (n+1) points $(P_0,P_1,\ldots,P_n)$ that define the current simplex in n-dimensional space with points that yield progressively smaller function values $(f_0,f_1,\ldots,f_n)$ at the new vertex points. A graphic illustration of how the method works is shown in Fig. 9 for a hypothetical function, f, of two variables, C_1 and C_2. In the figure, a triangle with vertices on the function surface represents a possible simplex. In the optimization process, the triangle (simplex) flip-flops down the function valley, expanding if possible to speed up the process, then contracting when it straddles the minimum.

To use the simplex method for optimizing waverider L/D, the shape of the forward projection of the leading edge must be parameterized in some general way. In the present work, five points in the x-y plane, lying inside of the shock domain, were chosen to represent the forward leading edge projection. A cubic spline-fit through the five points is then used to generate a continuous leading edge. One of the five points, the symmetry plane point, is constrained to lie on the y-axis, hence its x- value is always zero. This leaves nine variables, the remaining x and y values of the leading edge projection points, for the optimization routine to manipulate in search of an optimum waverider. A set of leading edge coordinates thus represent a single vertex point,

$$P_i = (x_2,x_3,x_4,x_5,y_1,y_2,y_3,y_4,y_5)_i \qquad (49)$$

of the required simplex, where $x_1 = 0$ as explained, and the function to be minimized is the negative of the lift-to-drag ratio

$$f_i(P_i) = (-L/D)_i \qquad (50)$$

Note that the five leading edge points are used to define only half of the projected leading edge shape, since the other half is constrained by vehicle symmetry to be the mirror image of the first half.

With nine variables (n=9), ten points (hence ten leading edge shapes) must be chosen to create the initial simplex. In the present work, five polynomials of the form

$$y_{\ell e} = C_1 + C_2 x_{\ell e} + C_3 x^2 \qquad (51)$$

and five cosine curves of the form

$$y_{\ell e} = C_4 + C_5 \cos\left(C_6 \frac{\pi}{2} \frac{x_{\ell e}}{r_s}\right) \qquad (52)$$

were used to describe the initial leading edge shapes; the constants $C_1,C_2,\ldots C_6$ being varied to generate a set of distinct shapes. An example of a set of initial leading edge shapes is shown in Fig. 10 -- the bold line representing the final shape associated with the optimum waverider for this case. Also note that in the present work, 100 steps of the optimization routine were executed for all cases run, though a convergence criterion could have been implemented as described in Ref. 17. It was found that one-hundred steps provided adequate convergence for engineering accuracy ($\sim 10^{-3}$-10^{-4}) without using excessive computer resources to generate an optimized waverider.

For more details on the optimization scheme, see Ref. 7.

III. RESULTS AND DISCUSSION

The present results are divided into four sections, as follows: (1) a presentation of optimum waverider shapes and aerodynamic characteristics at Mach 6 and 25, representing two extremes of the hypersonic flight spectrum; (2) a numerical experiment to assess the impact of boundary layer transition on the optimized waverider shapes; (3) an assessment of the need to account for detailed surface variations of shear stress in contrast to the use of an average skin friction coefficient during the optimization process; (4) an examination of the question: if the skin friction is deleted from the present analysis, what type of optimized inviscid waverider configuration is produced?

Due to the specialized nature of any waverider generation analysis, including the present one, it is difficult to obtain a direct benchmark comparison with existing data in order to verify the integrity of the current results. However, with the present analysis, it is possible to calculate the aerodynamic properties of a half-cone with a flat delta wing mounted on top; in this case the wing will have a sweep angle corresponding to the shock angle of the cone, and the body will be at zero degrees angle of attack. This specialized case was calculated at Mach 6.8 for a half-cone of $\theta_c = 3.67°$, and the corresponding wing sweep angle of 81°. The result is given as the flagged solid square in Fig.3. This is to be partly compared with the point labeled P2a, which was obtained from Ref. 3, and which corresponds to a similar flat-top half-cone, delta wing model, but at conditions of maximum L/D, hence at some positive angle of attack. About the only point to be made here is that the calculated L/D at zero angle of attack is lower than the measured $(L/D)_{max}$ at some angle-of-attack -- a proper qualitative result. The measured L/D at zero angle-of-attack is not presented in Ref. 3; however, through a personal inquiry to Patrick Johnston at NASA Langley, the present authors have been told that the measured L/D at zero-angle-of-attack was 2.7 -- about eight percent higher than the value of 2.5 calculated with the present analysis. This is a reasonable comparison, and if anything, seems to indicate that the present aerodynamic analysis is conservative. (Please note that the comparisons discussed above are for a given configuration, not an optimized waverider; hence any degree of

of validation here pertains to the aerodynamic portion of the analysis and not to the present optimization process itself.)

A. Representative Waveriders

In Ref. 7, a series of optimized waveriders is generated, including cases at M_∞ = 4,6,10,15,20 and 25. The conditions correspond to altitude-velocity points along a typical entry flight trajectory of a lifting hypersonic vehicle, such as an aerospace plane. In the present section, only the results at M_∞ = 6 and 25 are presented as representative of the two extremes of the flight spectrum. Ref. 7 should be consulted for additional results.

Fig. 11 gives values of (L/D), C_L, and volumetric efficiency, $\eta = V^{2/3}/S_p$, for waveriders optimized at different assumed wave angles for the conical shock. To understand this more fully, consider the conical flow field associated with a given conical shock wave, say θ_s = 11°. For this value of θ_s an optimum waverider shape is obtained (refer again to the bold curve in Fig. 10). The resulting characteristics of this optimized waverider are then plotted on Fig. 11 for θ_s = 11°. This process is repeated for other values of θ_s, say 12°, 13°, and 14°. For each value of θ_s, an optimized waverider is obtained, and its characteristics plotted in Fig. 11 as the open symbols. (The solid symbols will be discussed later.) Hence, Fig. 11 pertains to an entire series of optimized waveriders. However, note that the (L/D) curve itself has a maximum (in this case for θ_s = 12°). This yields an "optimum of the optimums", and defines the final viscous optimized waverider at M_∞ = 6 for the flight conditions shown in Fig. 11. The front views of the optimum shapes at each value of θ_s are shown in Fig. 12, and the corresponding perspective views are shown in Fig. 13. Finally, a summary three-view of the best optimum (the "optimum of the optimum") waverider, which here corresponds to θ_s = 12°, is given in Fig. 14. Also in Figs. 12-14, the lines on the upper and lower surfaces of the waveriders are inviscid streamlines. Note in these figures that the shape of the optimum waverider changes considerably with θ_s. Moreover, examining (for example) Figure 14, note the rather complex curvature of the leading edge in both the planform and front views; the optimization program is shaping the waverider to adjust both wave drag and skin friction drag so that the overall L/D is a maximum. Indeed, it was observed in all of the present results that the best optimum shape at any given M_∞ results in the magnitudes of wave drag and skin friction drag being approximately the same, never differing by more than a factor of two. For conical shock angles below the best optimum (for example θ_s = 11° in Figs. 12 and 13), skin friction drag is greater than wave drag; in contrast, for conical shock angles above the best optimum (for example θ_s = 13° and 14° in Figures 12 and 13), skin friction drag is less than wave drag. (Note: For a hypersonic flat plate, using Newtonian theory and an average skin friction coefficient , it can readily be shown that at maximumum L/D, the wave drag is twice the friction drag.)

The results in Figs. 11-14 pertain to M_∞ = 6. An analogous set of results for the other extreme of the lifting hypersonic flight spectrum at M_∞ = 25 is given in Figs. 15-18. The aerodynamic characteristics of optimum waveriders for θ_s = 7°,8°,9° and 10° are given as the open symbols Fig. 15 (the solid symbols will be discussed later.) The respective front views are shown in Fig. 16, and perspective views in Fig. 17. Finally, the best optimum Mach 25 waverider (which occurs at θ_s = 9°) is summarized in Fig. 18. Comparing the optimum configuration at M_∞ = 6 (Fig. 14) with the optimum configuration at Mach 25 (Fig. 18), note that the Mach 25 shape has more wing sweep, and pertains to a conical flowfield with a smaller wave angle, both of which are intuitively expected at higher Mach number. However, note from the flight conditions listed in Figs. 11 and 15 that the body slenderness ratio at M_∞ = 6 is constrained to be b/ℓ = 0.06 (analogous to a supersonic transport such as the Concorde) but that b/ℓ = 0.09 is the constraint chosen at M_∞ = 25 (analogous to a hydrogen fueled hypersonic aeroplane such as the British HOTOL). The two different slenderness ratios are chosen on the basis of reality for two different aircraft with two different missions at either extreme of the hypersonic flight spectrum. Also note in Figs. 16-18 the optimization program has sculptured a best optimized configuration with a spline down the center of the upper surface--an interesting and curious result, due principally to the competing effects of minimizing pressure and skin friction drag, while meeting the slenderness ratio constraint.

Return to Fig. 15, and note the solid symbols. These pertain to the values of C_L and L/D obtained by setting the ratio of specific heats γ to 1.1 in order to assess possible effects of high temperature chemically reacting flow. The solid symbols pertain to an optimized waverider at θ_s = 9° with γ = 1.1. This is not necessarily the best optimum at Mach 25 with γ = 1.1; rather, it is just a point calculation to indicate that high temperature effects will most likely have a significant impact on optimized waverider generation, and that such effects are worthy of future investigation. The detailed aspects of high temperature effects are beyond the scope of the present paper; additional discussion is given in Ref. 7.

As a final note in this section, return to Fig. 3, and note that the solid symbols pertain to the present investigation. The flagged square has been discussed earlier as the data point for a half-cone with a delta wing at zero angle-of-attack; it is not part of the present waverider family. The unflagged solid square at M_∞ = 4 pertains to a relatively large slenderness ratio of 0.087, used to generate a waverider for wind tunnel testing. The remaining solid symbols, the circles and triangles, pertain to the present discussion. Recall that the circles are for b/ℓ = 0.06 (a Concorde-like slenderness ratio for a low Mach number configuration), and that the triangles are for b/ℓ =0.09 (a HOTOL-like slenderness ratio for a high Mach number configuration). In the present section, we have discussed results obtained at Mach 6 and 25; Fig. 3 shows these plus others at intermediate Mach numbers. All of these cases are discussed in detail in Ref. 7. However, in regard to Fig.3, emphasis is now made that the present viscous optimized waveriders produce values of (L/D) which exceed the "L/D barrier" discussed in Section I, and shown as the solid curve in Fig.3. Indeed, the present waverider L/D variation is more closely given by

$$(L/D)_{max} = \frac{6(M+2)}{M}$$

shown as the dashed curve in Fig. 3. Note that the two points given for M_∞ = 20 and 25 deviate away from the dashed curve. This is a Reynolds number effect. Recall that all the Mach number-altitude points for the present waveriders are chosen to follow a typical lifting vehicle flight path through the atmosphere. The point at Mach 25 is at very high altitude (250,000 ft.), with a corresponding low Reynolds number ($Re = 1.4 \times 10^6$); the flow is completely laminar. At Mach 20, the Reynolds number is 12 times higher, but based on the transition criterion discussed in Section II the flow is still completely laminar. Hence, the laminar skin-friction coefficient at the Mach 20 point in Fig. 3 is much lower ($c_f \propto 1/\sqrt{Re}$) than at the Mach 25 point, with an attendant larger (L/D) at Mach 20. In contrast, the point at Mach 15 is transitional, with regions of both laminar and turbulent flow, and hence with larger skin-friction and a lower (L/D). In any event, the results given in Fig. 3 indicate that the present viscous optimized waveriders produce high values of (L/D), and therefore are worthy of additional consideration for hypersonic vehicle application.

B. Sensitivity to Transition

Because the major thrust of the present work is the inclusion of detailed viscous effects in the waverider optimization, the question naturally arises: How sensitive are the present waveriders to uncertainties in the location of transition from laminar to turbulent flow? To address this question, a numerical experiment is carried out wherein the transition location was varied over a wide latitude, ranging from all laminar flow on one hand, to almost all turbulent flow on the other hand, with various cases inbetween. Specific results at Mach 10 are given in Fig. 19; here values of (L/D) are given for optimized waveriders as a function of assumed transition location. The point corresponding to the transition correlation described in Section II, D.3, is denoted by "x" in Fig. 19. Other points in Fig. 19 labeled 5x, 10x and 15x correspond to transition locations that are 5, 10 and 15 times the value predicted by the transition correlation. All the data given in Fig. 19 pertain to optimized waveriders for $\theta_s = 9°$, which yields the best optimum at Mach 10 for the usual transition correlation. (Note, however, that $\theta_s = 9°$ may not yield the best optimum for other transition locations; this effect is not investigated here.) The results in Fig. 19 demonstrate a major increase in (L/D) in going from almost all turbulent flow to all laminar flow. However, for the case where transition is changed by a factor of five, only a 2% change in L/D results. Even for the case where transition is changed by a factor of ten, a relatively small change in L/D of 11% results. On the other hand, the shapes of the resulting optimized waveriders are fairly sensitive to the transition location, as illustrated in Figs. 20 and 21. The conclusion to be made here is that waverider optimization is indeed relatively sensitive to transition location, and this underscores the need for reliable predictions of transition at hypersonic speeds.

C. On the Use of Average Skin Friction Coefficients

The present detailed viscous analysis computes the surface shear stress distributions, and integrates over the surface to obtain the total skin friction drag. This requires a substantial amount of computer calculations, and leads to the question: Can an overall average skin friction coefficient be used within the optimization process rather than dealing with the detailed shear stess distributions? To address this question, consider the best optimum Mach six case given in Fig. 11, which was orginally calculated with the detailed shear stress distributions. From this result, an average skin friction drag coefficient was calculated for the complete configuration. Then the optimization code was run again for the same Mach six case, now using this average skin friction drag coefficient. The results are given in Fig. 11 as the solid symbols. Only a small difference exists between the two cases; indeed, the resulting waverider shapes are virtually the same, as given in Ref. 7. This implies that if an accurate average skin friction drag coefficient can be obtained, the resulting optimized waveriders would be reasonably valid. However, the problem with this method is that the information needed to obtain the average skin friction drag coefficient is not known apriori. Moreover, if other independent means are used to obtain an approximate average skin friction drag coefficient and this approximate average value is used in the optimization process, the results can be quite different from those obtained from the use of detailed shear stress distributions; see Ref. 7 for more discussion on this aspect. This situation, in combination with the sensitivity to transition demonstrated in the previous section, seems to dictate the necessity of using the detailed shear stress distributions rather than some approximate average value of skin friction drag coefficient for obtaining the proper optimized waveriders.

D. Inviscid Optimized Waveriders

As a final note, it is interesting to pose the question: if the skin friction is deleted from the present analysis, what type of optimized inviscid waverider configuration, with a constraint on slenderness ratio, is produced? To examine this question, the present computer code was run without skin friction as part of the optimization process, covering the range of Mach number from 6 to 25. A typical result for the inviscid optimized configuration is shown in Fig.22. Here we see essentially a wedge-like caret waverider, such as the classic configuration generated by the two-dimensional flow behind a planar oblique shock wave, as discussed by Nonweiler[8,9]. This clearly indicates that the optimized inviscid waverider with slenderness ratio as the constraint is indeed a caret wing. The result shown in Fig. 22 is produced by the present conical flow analysis as a "limiting case", wherein the optimum shape is seeking the flattest portion of the conical shock wave. To see this more clearly, return to Fig. 6. The resulting inviscid waveriders are being generated by relatively flat streamsurfaces at the extreme back and bottom of the generating conical flow-field -- where the shock radius of curvature is the largest and the flow is closest to being two-dimensional. Consequently, the inviscid configurations are tiny

shapes compared to the scale of the flowfield in Fig. 6, and they are "squeezed" into a tiny area at the bottom of the shock base. In turn, due to the logic of the existing conical flow code, only a few pressure and shear stress points are calculated on the surface of these tiny waveriders, raising questions about the numerical accuracy of the calculation of their lift and drag. Therefore, no further discussion about the inviscid optimized waveriders will be given here, except to emphasize again that a two-dimensional caret wing seems to be the optimum inviscid shape that is predicted by the present conical flow analysis.

IV CONCLUSIONS

In comparison to previous optimized waverider analyses, the present work is the first to include detailed viscous effects within the optimization process. From this work, the following major conclusions are made:

1. The resulting family of viscous hypersonic waveriders yields predicted high values of (L/D) which break the "L/D barrier" discussed in Section I.
2. The optimization process for the viscous waveriders results in distinctly different shapes compared to previous work with inviscid-designed waveriders.
3. The fine details of the viscous solution, such as how the shear stress is distributed over the surface, and the location of transition, are crucial to the details of the resulting waverider geometry.

V. ACKNOWLEDGEMENT

This work was supported through the Graduate Hypersonic Aerodynamics Fellowship Program, established in 1983 at the University of Maryland by the Army Research Office, with Dr. Robert Singleton as monitor. The authors also acknowledge a close working relationship with the Fundamental Aerodynamics Branch at the NASA Langley Research Center under a grant monitered by Wallace Sawyer and Patrick Johnston.

REFERENCES

1. Anderson, John D. Jr., "A Survey of Modern Research in Hypersonic Aerodynamics," AIAA Paper No. 84-1578. Invited paper given at the AIAA 17th Fluid Dynamics, Plasma Dynamics, and Lasers Conference, Snowmass, Colorado, June 25-27, 1984.

2. Anderson, John D., Jr., "Hypersonic Aerodynamics," notes printed by the AIAA for the Short Course presented in Atlanta, Georgia, May 10-11, 1986.

3. Fetterman, D.E., Henderson, A., Jr., Bertram, M.H., and Johnston, P.J., "Studies Related to the Attainment of High Lift-Drag Ratios at Hypersonic Speeds," NASA TN D-2956, August 1965.

4. Penland, J.A., Marcum, D.C., Jr., and Stack, S.H., "Wall-Temperature Effects on the Aerodynamics of a Hydrogen-Fueled Transport Concept in Mach 8 Blowdown and Shock Tunnels," NASA TP 2159, July 1983.

5. Loftin, Laurence, Quest for Performance; The Evolution of Modern Aircraft, Pergamon Press, Oxford, 1978, pp. 448-510.

6. Kuchemann, D., The Aerodynamic Design of Aircraft, Pergamon Press, Oxford, 1978, pp.448-510.

7. Bowcutt, Kevin G., Optimization of Hypersonic Waveriders Derived from Cone Flows -- Including Viscous Effects, Ph.D. Dissertation, Dept. of Aerospace Engineering, University of Maryland, College Park, Maryland, 1986.

8. Nonweiler, T.R.F., "Aerodynamic Problems of Manned Space Vehicles," Journal of the Royal Aeronautical Society, Vol. 63, 1959, pp. 521-528.

9. Nonweiler, T., "Delta Wings of Shapes Amenable to Exact Shock-Wave Theory," Journal of the Royal Aeronautical Society, Vol. 67, Jan. 1963, pp.39-40.

10. Townend, L.H., "Research and Design for Lifting Reentry," Progress in Aerospace Sciences, Vo. 18, 1979, pp. 1-80.

11. Jones, J.G., Moore, K.C., Pike, J., and Roe, P.L., "A Method for Designing Lifting Configurations for High Supersonic Speeds, Using Axisymmetric Flow Fields," Ingenieur-Archiv, Vol. 37, 1968, pp.56-72.

12. Rasmussen, M.L., "Waverider Configurations Derived from Inclined Circular and Elliptic Cones," J. of Spacecraft and Rockets, Vol. 17, No.6, Nov.-Dec., 1980, pp. 537-545.

13. Rasmussen, M.L., and Clement, L.W., "Cone-Derived Waveriders With Longitudinal Curvature," AIAA Paper No. 84-2100, 1984.

14. Cole, J.D. and Zien, T.F., "A Class of Three-Dimensional, Optimum Hypersonic Wings," AIAA Journal, Vol. 7, No. 2, Feb. 1969, pp.264-271.

15. Kim, B.S., Rasmussen, M.L. and Jischke, M.C., "Optimization of Waverider Configurations Generated from Axisymmetric Conical Flows," AIAA Paper No. 82-1299, 1982.

16. Kim, B.S., Optimization of Waverider Configurations Generated from Non-Axisymmetric Flows Past a Nearly Circular Cone, Ph.D. Dissertation, School of Aerospace, Mechanical, and Nuclear Engr., Univ. of Oklahoma, 1983.

17. Nelder, J.A. and Mead, R., "A Simplex Method for Function Minimization," Computer Journal, Vol.7, Jan. 1965, pp. 308-313.

18. Anderson, John D., Jr., Modern Compressible Flow: With Historical Perspective, McGraw-Hill, New York, 1982.

19. Forsythe, G.E., Malcom, M.A. and Moler C.B., Computer Methods for Mathematical Computations, Prentice-Hall, Inc., New Jersey, 1977.

20. Flower, J.W., "Configurations for High Supersonic Speeds Derived from Simple Shock Waves and Expansions," Journal of the Royal Aeronautical Society, Vol. 67, 1963, p. 287.

21. Moore, K.C., "The Application of Known Flow Fields to the Design of Wings with Lifting Upper Surfaces at High Supersonic Speeds," R.A.E. Tech. Rept. No. 65034, ARC 26913, Feb. 1965.

22. Ferri, A., General Theory of High Speed Aerodynamics, Princeton Series, Sears, W.R. (Editor), Vol. 6, 1954, pp.616-623.

23. Nonweiler, T., Wong, H.Y., and Aggarwal, S.R., "The Role of Heat Conduction in Leading Edge Heating," Ingenieur-Archiv, Vol. 40, 1971, pp. 107-117.

24. Walz, A., Boundary Layers of Flow and Temperature, M. I. T. Press, Cambridge, Mass., 1969.

25. White, F.M., Viscous Fluid Flow, McGraw-Hill, New York, 1974, pp. 653-657.

26. DiCristina, V., "Three-Dimensional Laminar Boundary-Layer Transition on a Sharp 8° Cone at Mach 10", AIAA Journal, Vol. 8, No. 5, May 1970, p. 855.

27. Pate, S.R., and Groth, E.E., "Boundary-Layer Transition Measurements on Swept Wings with Supersonic Leading Edges," AIAA Journal, Vol.4, No.4, April 1966, pp. 737-738.

28. Harris, J.E., and Blanchard, D.K., "Computer Program for Solving Laminar, Transitional, and Turbulent Compressible Boundary Layer Equations for Two Dimensional and Axisymmetric Flows," NASA TM 83207, Feb. 1982.

29. Christoph, G. H., "Law-of-the-Wall Analysis Revisited for Reentry Vehicle Design," AIAA Paper 85-0905, June 1985.

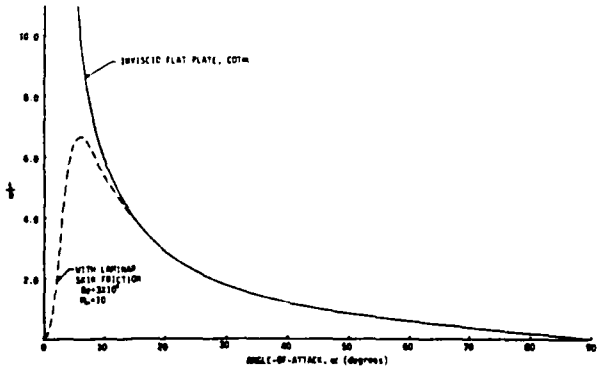

FIG 1: Newtonian results for a flat plate.

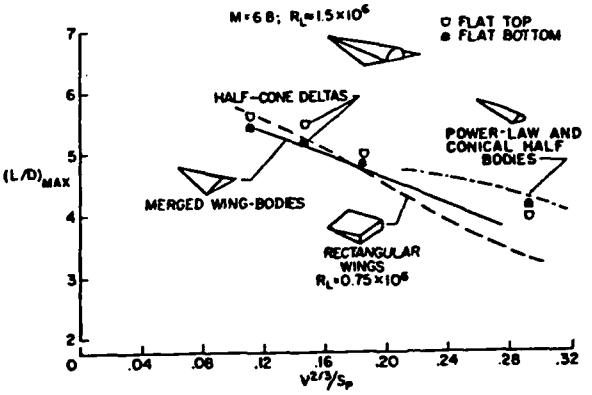

FIG. 2: Performance comparison of various generic hypersonic configurations (from Ref. 3).

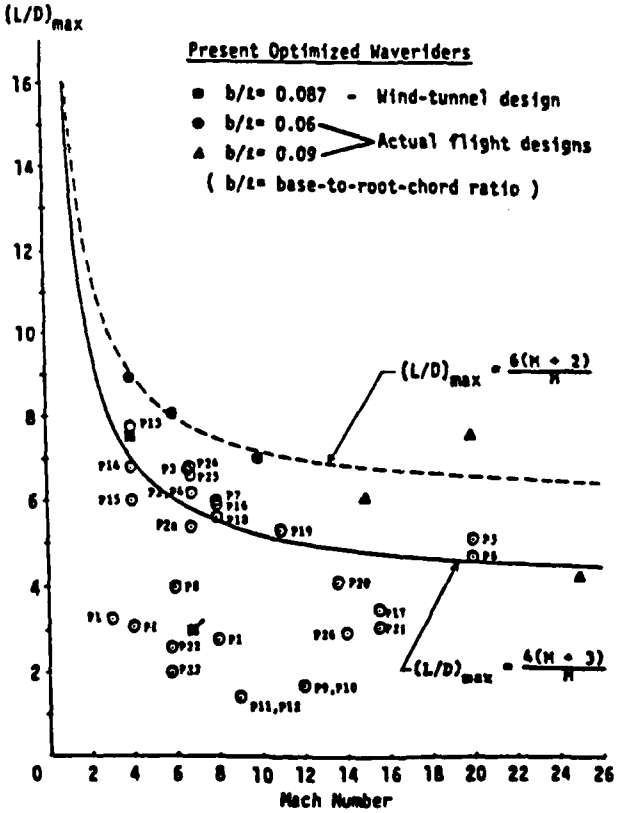

FIG 3: Maximum lift-to-drag ratio comparison for various hypersonic configurations.

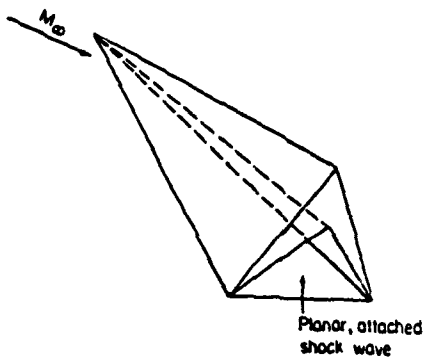

FIG 4: Schematic of a simple caret wing waverider.

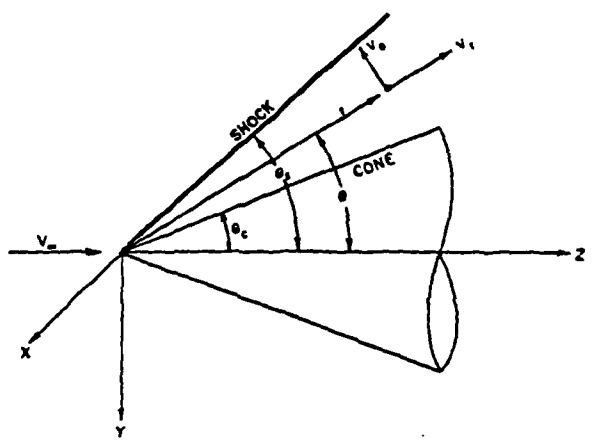

FIG. 5: Spherical coordinate system for cone flow calculations, and cartesian coordinate system for waverider design.

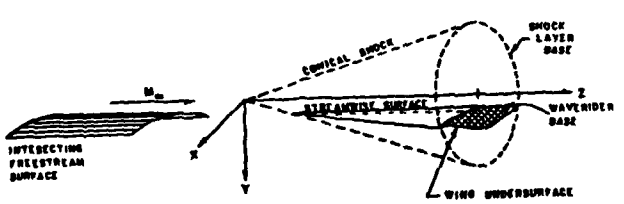

FIG 6: Perspective view of a conical waverider and generating shock.

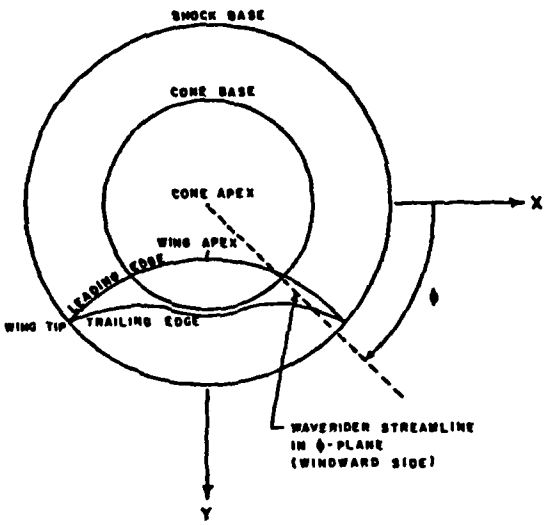

FIG. 7: Front view of a conical waverider with the generating cone and shock.

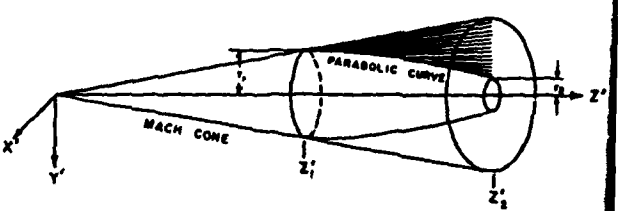

FIG 8: Expansion cylinder and expansion domain bounded by the Mach cone.

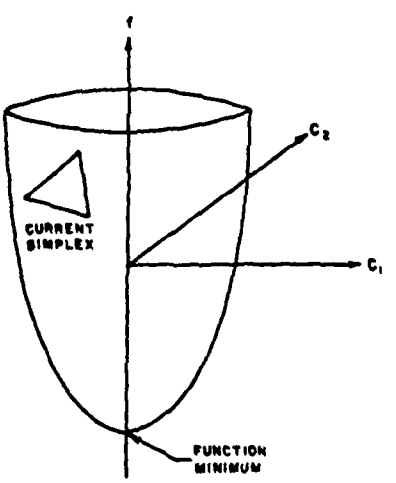

FIG. 9: Example of the optimization process for a function of two variables.

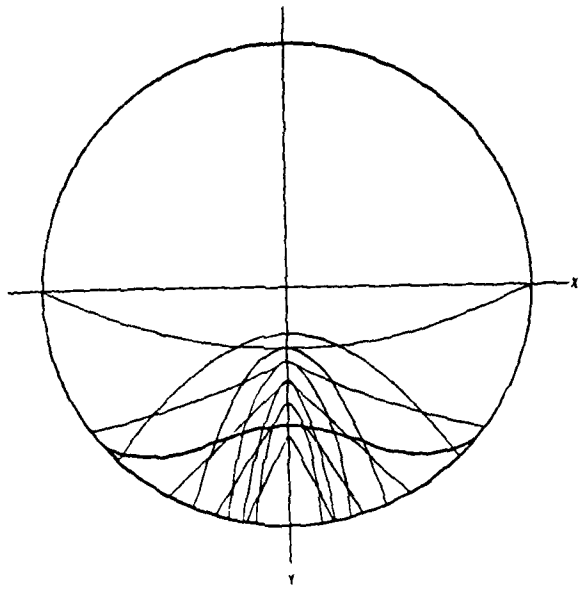

FIG. 10: Example of initial and optimized waverider leading edge shapes.

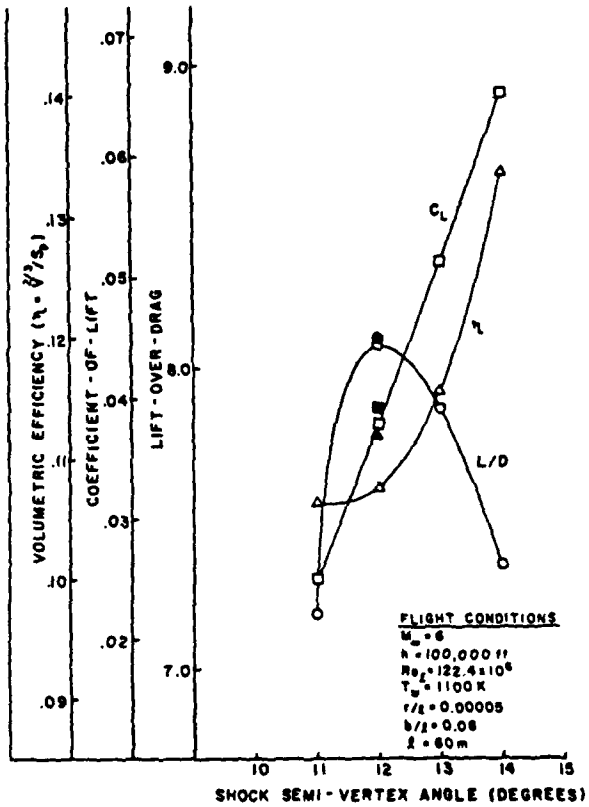

FIG. 11: Results for a series of optimized waveriders at Mach 6.

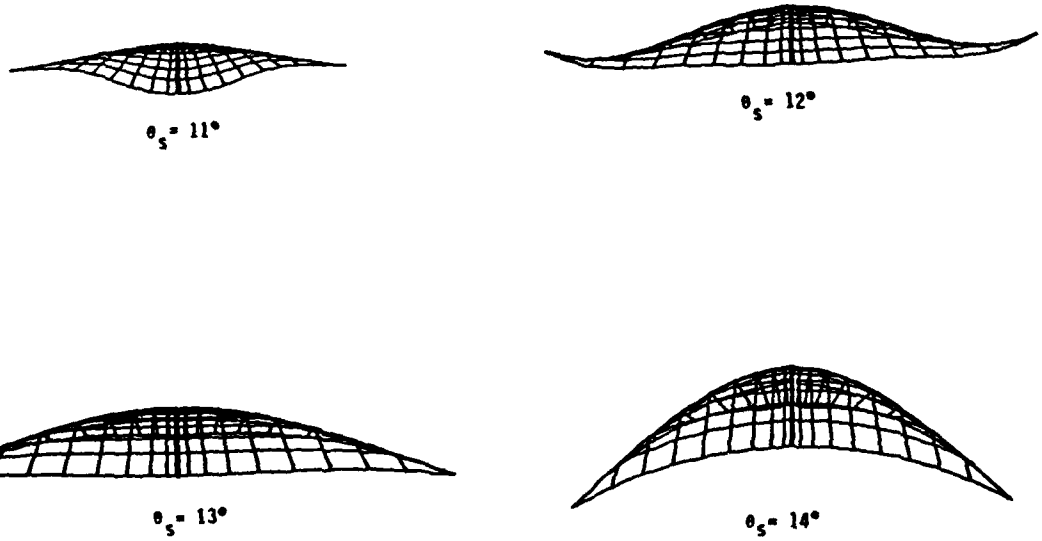

FIG 12: Front views of a series of optimized waveriders at Mach 6.

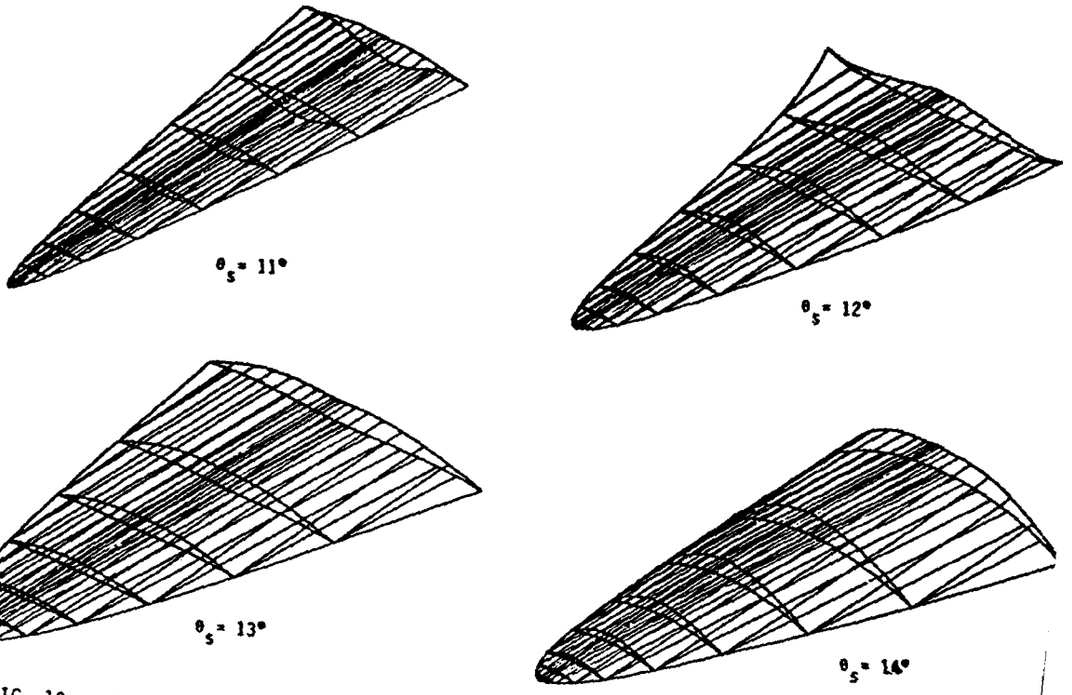

FIG. 13: Perspective views of a series of optimized waveriders at Mach 6.

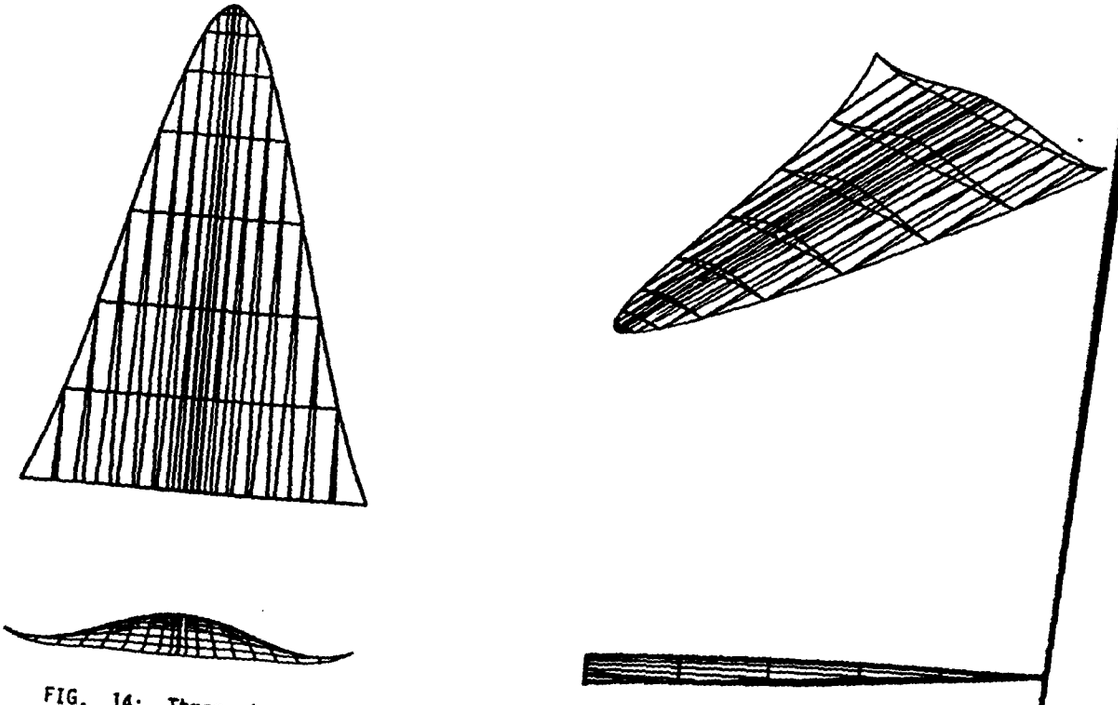

FIG. 14: Three-view of the best optimum waverider at Mach 6. (θ_s= 12°)

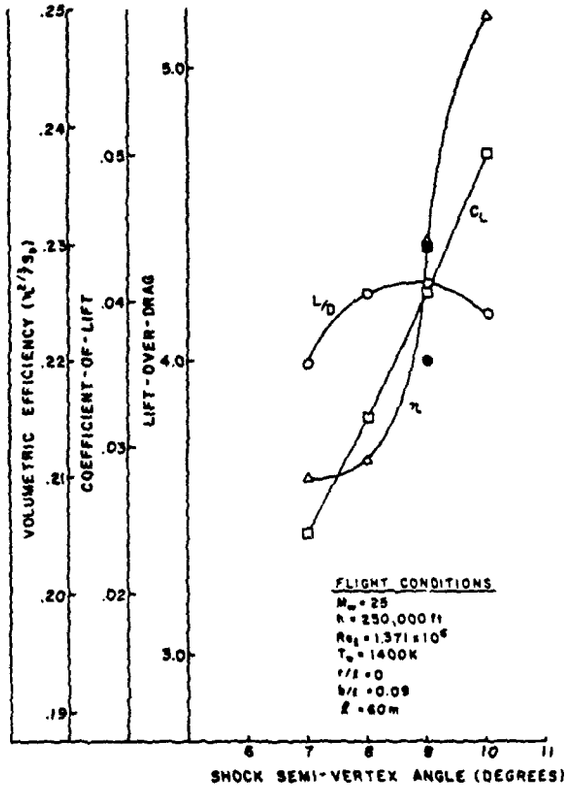

FIG. 15: Results for a series of optimized waveriders at Mach 25.

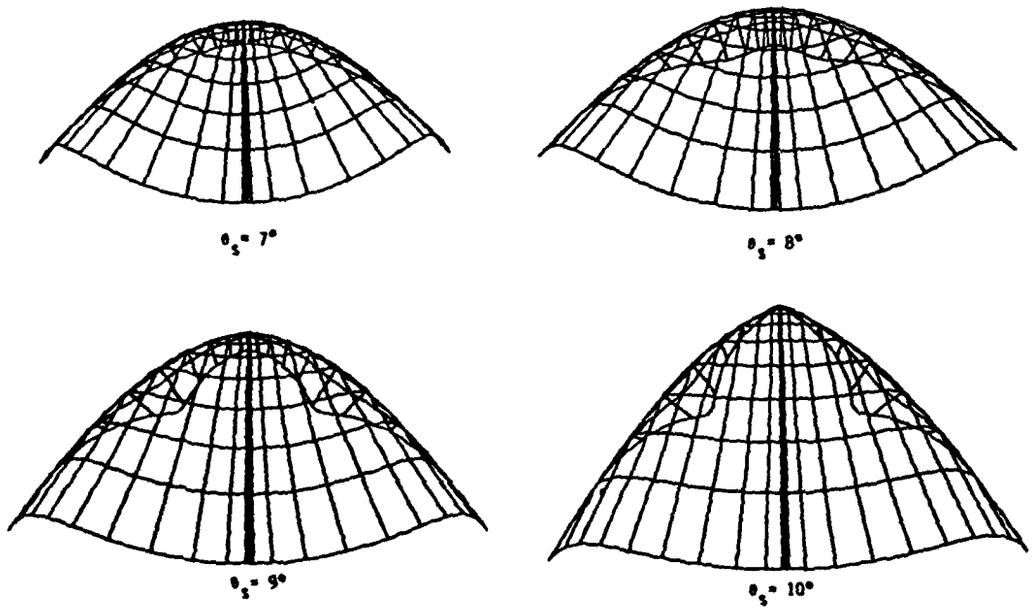

FIG. 16: Front views of a series of optimized waveriders at Mach 25.

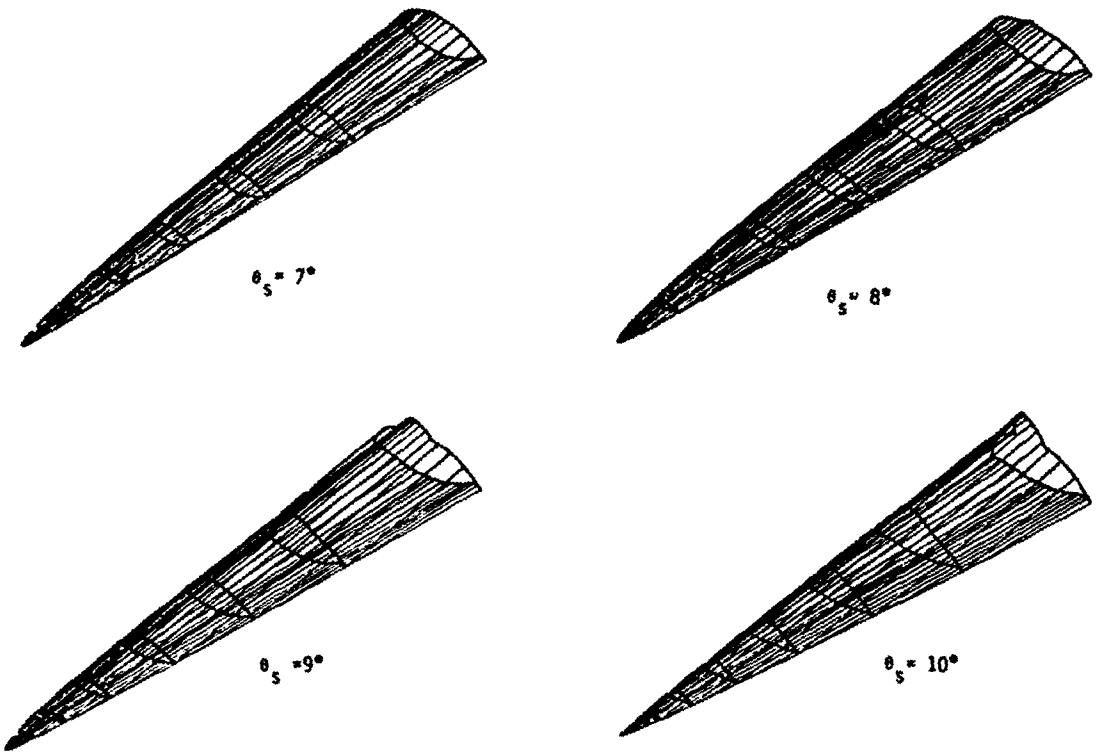

FIG. 17: Perspective views of a series of optimized waveriders at Mach 25.

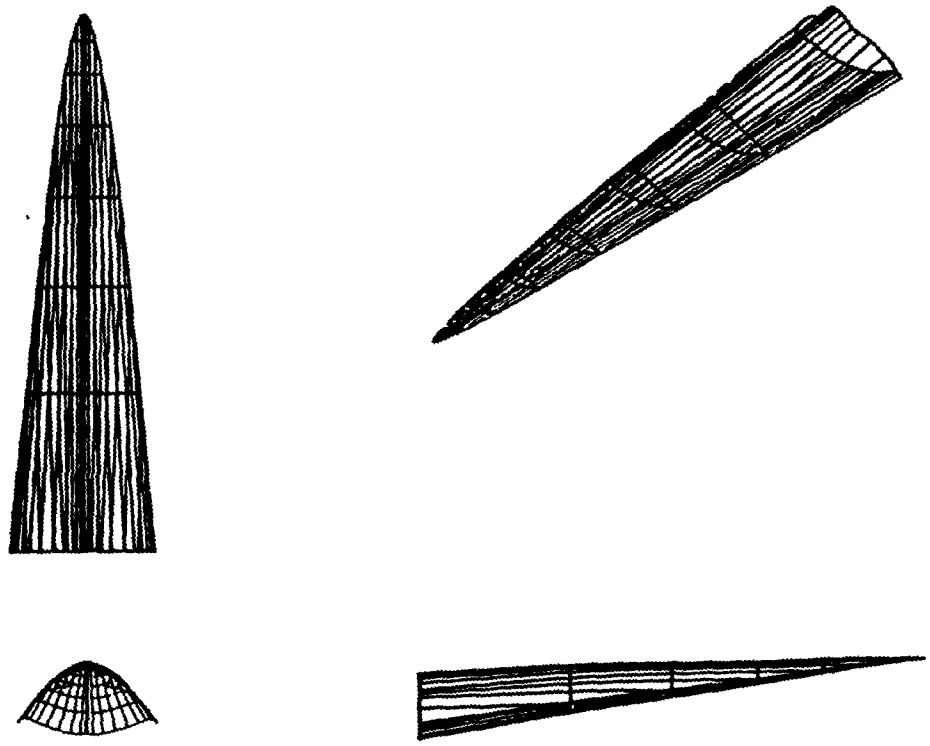

FIG. 18: Three-view of the best optimum waverider at Mach 25. (θ_s= 9°)

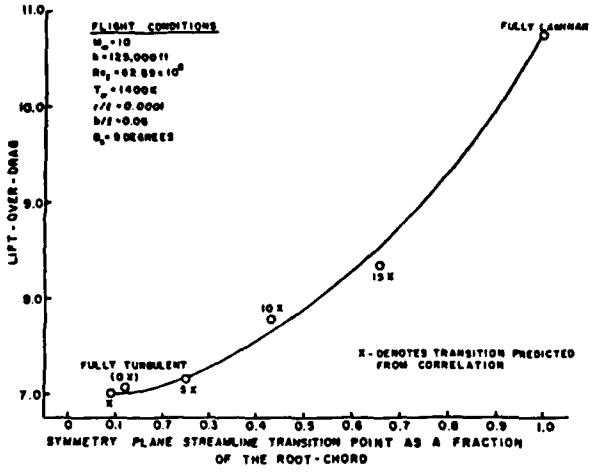

FIG. 19: Lift-to-drag comparison of optimized Mach 10 waveriders designed with various boundary layer transition criteria.

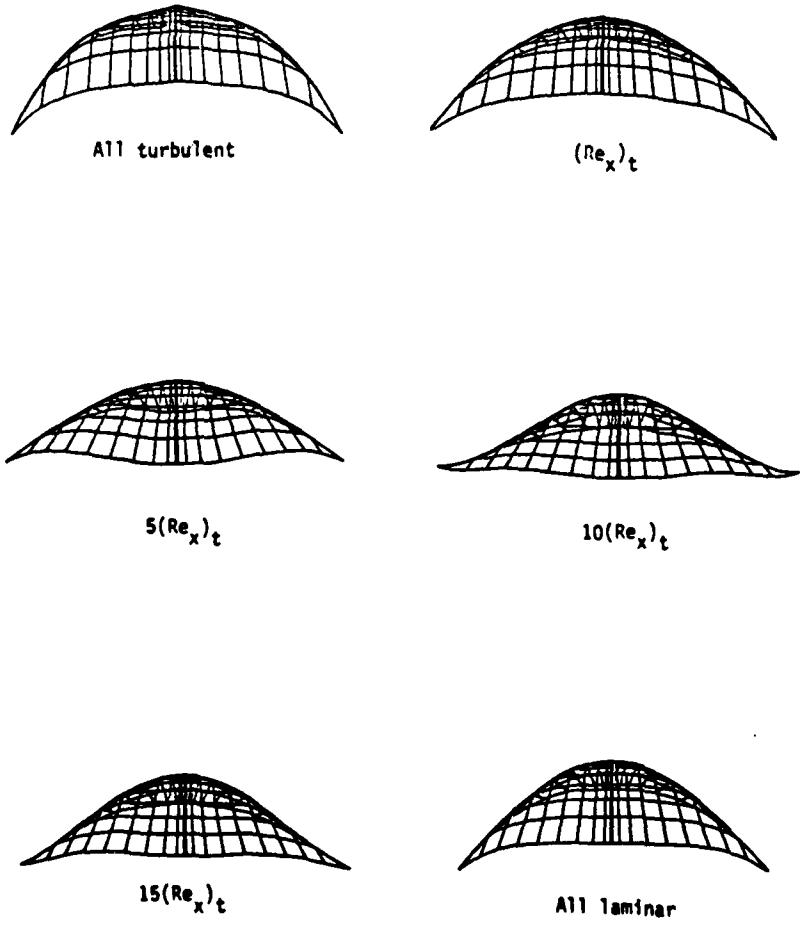

FIG. 20: Front views of optimized Mach 10 waveriders designed with various boundary layer transition criteria.

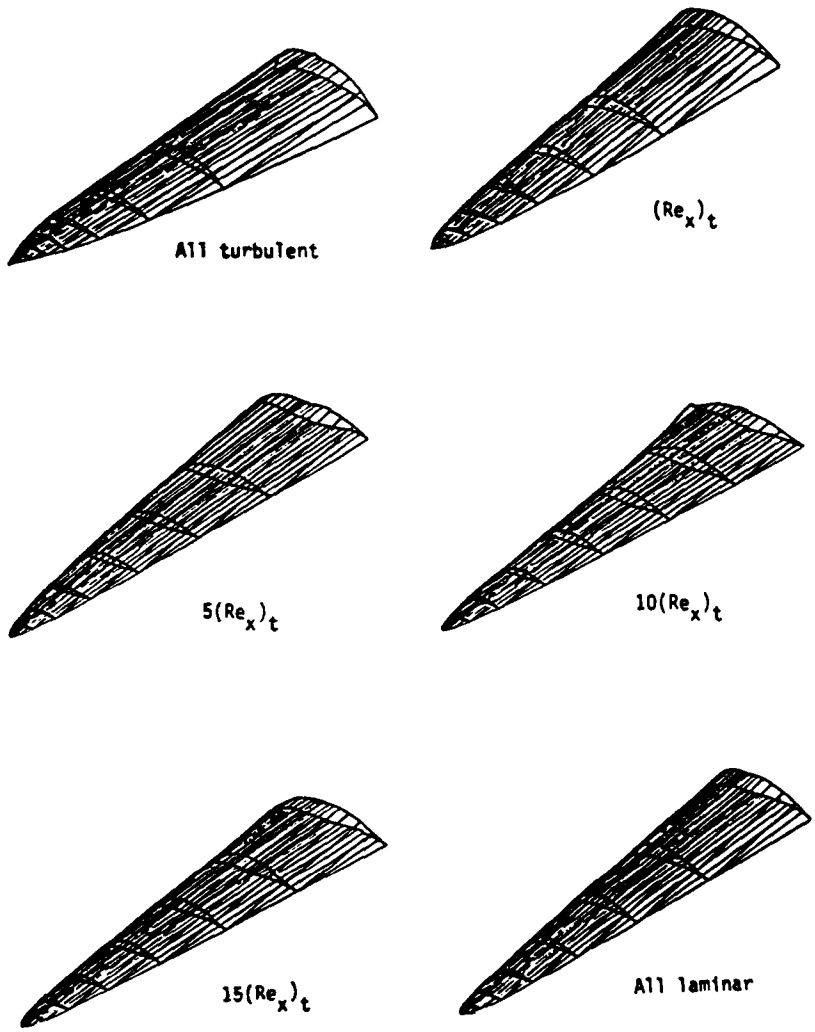

FIG. 21: Perspective views of optimized Mach 10 waveriders designed with various boundary layer transition criteria.

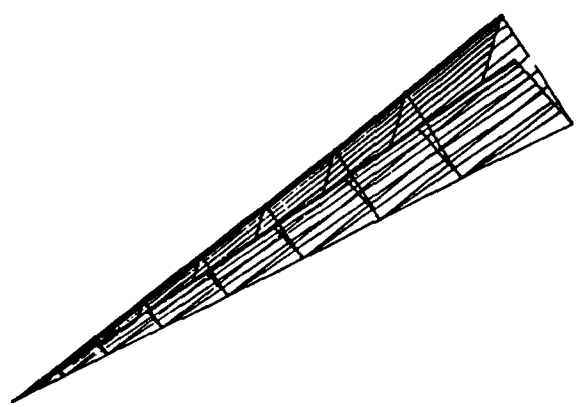

FIG. 22: An optimized inviscid waverider at Mach 10; a caret wing.

III. SHOCK WAVE/VORTEX INTERACTION

This research is the Ph.D. dissertation topic for Griffin Corpening, scheduled for completion in May, 1988. The problem involves the study of the interaction between an oblique shock wave and a vortex at hypersonic speeds. This is modeled as a three-dimensional inviscid flow. The solution technique involves the appliecation of computational fluid dynmaics; specifically, a time-marching, finite-volume approach is used, including upwind differencing. The computational method is patterned after that of Peter Gnoffo at the NASA Langley Research Center, and has been throughly tested for two-dimensional normal and oblique shocks, intersecting shocks, and slip lines intersecting oblique shocks. The three-dimensional method has not been tested as throughly due to computer time and memory constraints, but tests performed so far indicate the model to be operating properly.

In addition to the actual code development itself, it was necessary to write a number of programs to enable the flow field to be examined graphically. Due to the three-dimensionality, this was no trivial undertaking (on the order of three to four months was required to do this). The flow field can now be displayed by two-dimensional slices perpendicular to any of the three axes and at various locational stations along the axis. The two-dimensional slice can be reduced to contour plots, surface plots, velocity vector or streamline plots. Curves can also be plotted showing the velocity, density, etc. change through the slice. In addition, three-dimension streamlines can be calculated and plotted. All this combines to give a very flexible and complete way to graphically display the flowfield.

Some sample results are given as follows. (The figures are in a preliminary form which will be formalized for the dissertation.) The following figures depict a Mach 5 flowfield in which a vortex is interacting with a shock wave. The flowfield is depicted by showing a series of contour plots of density.

These plots are taken along planes which are perpendicular to the 3 axes. A Three-Dimensional Perspective figure is also included to help the reader orient the contour plots to the flowfield.

The freestream flow direction is in the positive X direction. The shock wave starts along the Z-axis at Y equal to 0 and proceeds up into the flow at an angle of 46.4 degrees to the X-Z plane and proceeds downstream.

3-D PERSPECTIVE

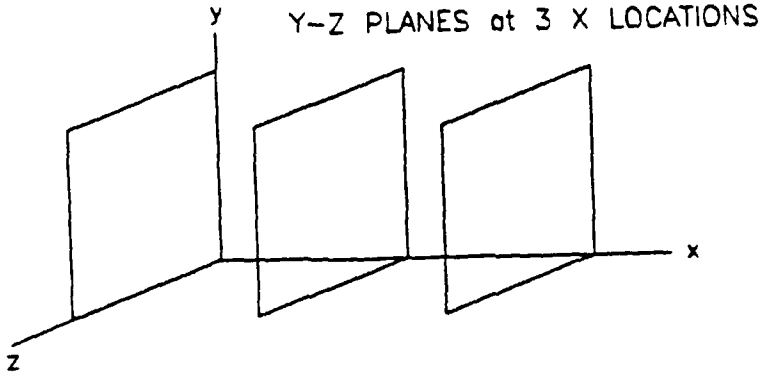

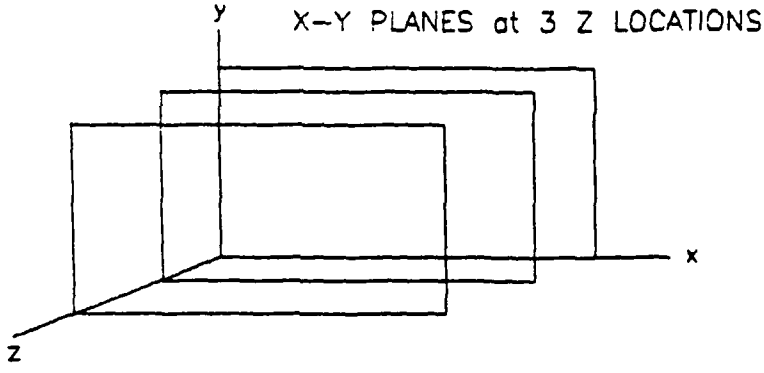

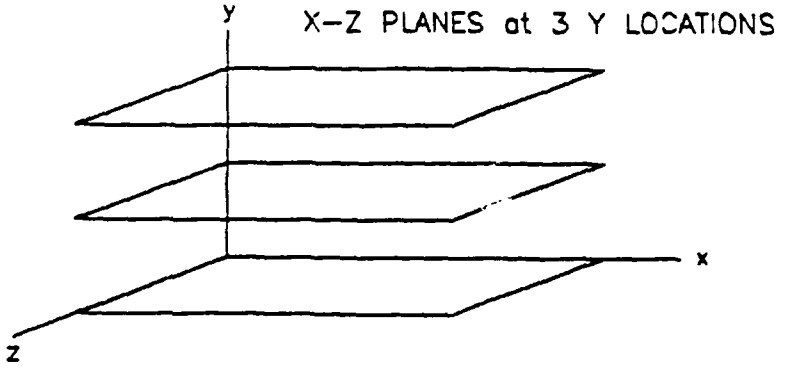

YZ FACE

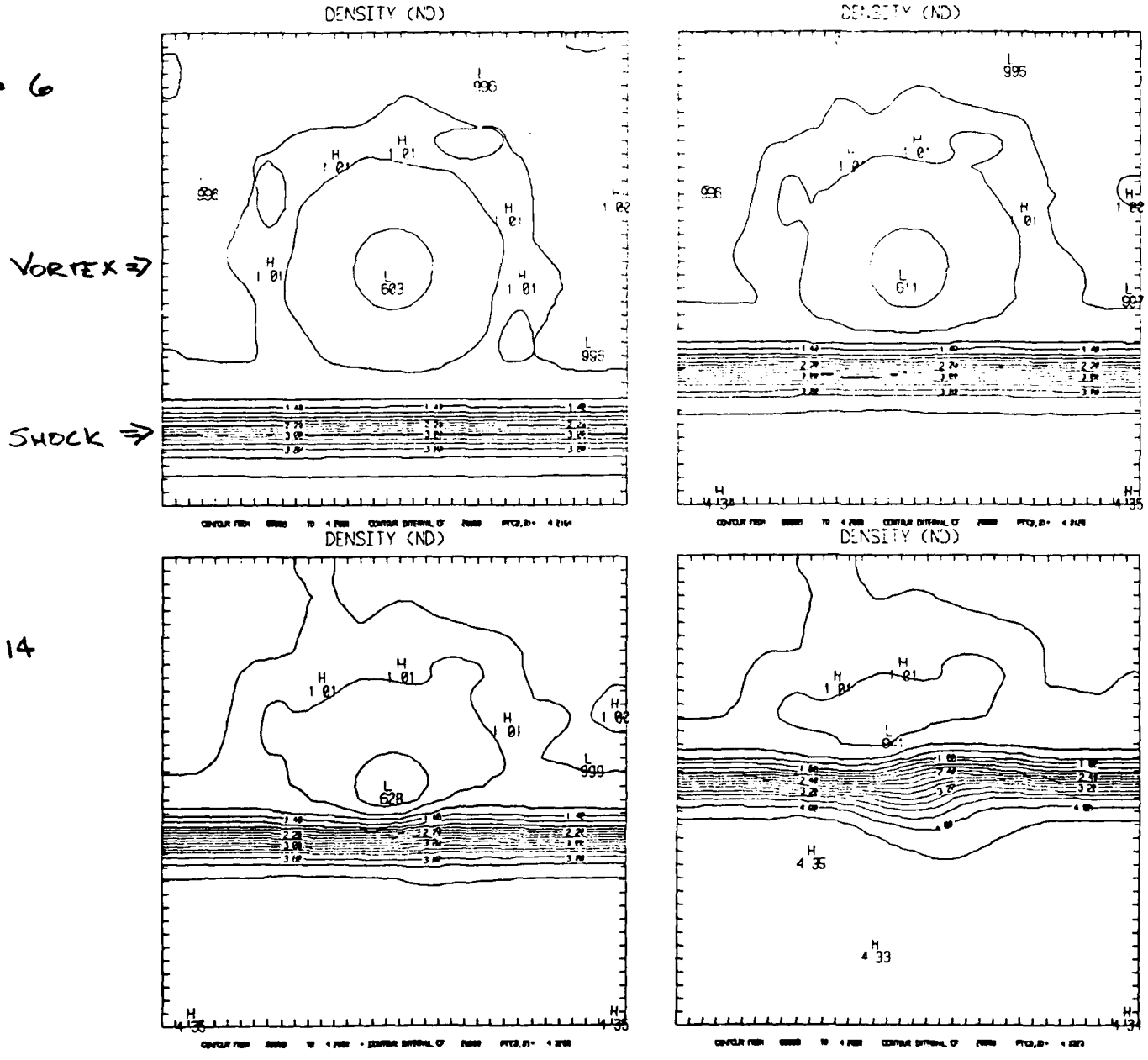

M S

SV1

YZ 6 10 14

YZ FACE

X = 22

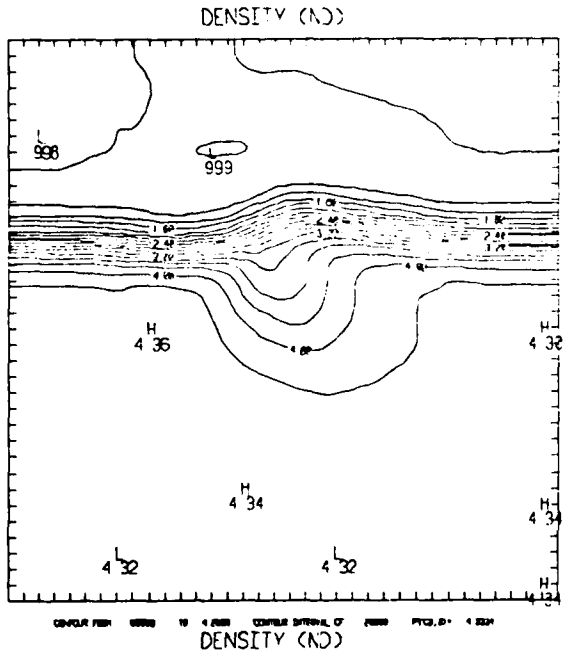

X = 26

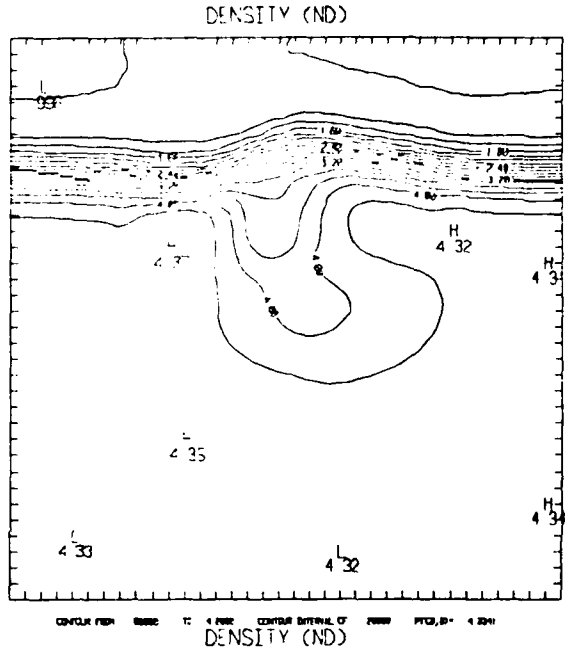

X = 30

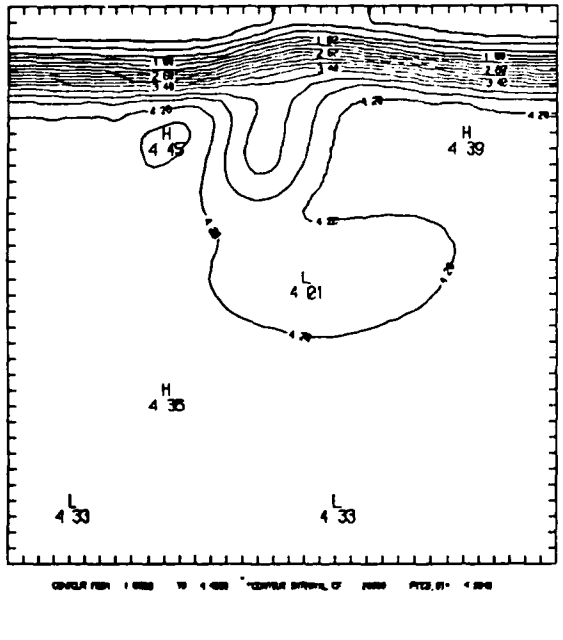

X = 34

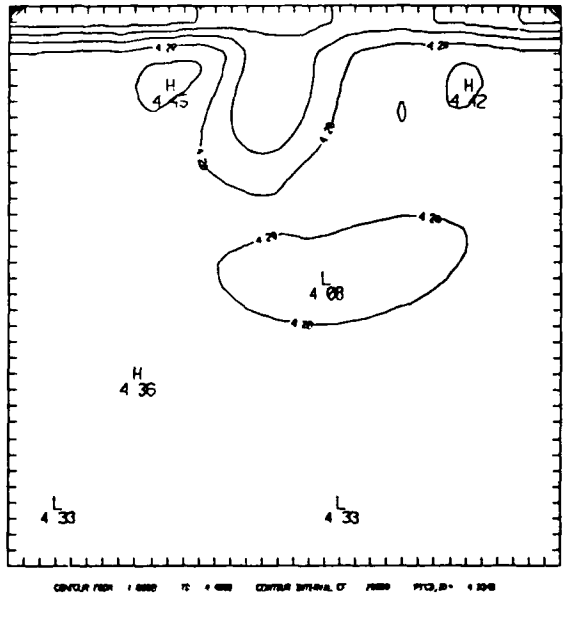

11.5

YZ 22 26 30

XY FACE

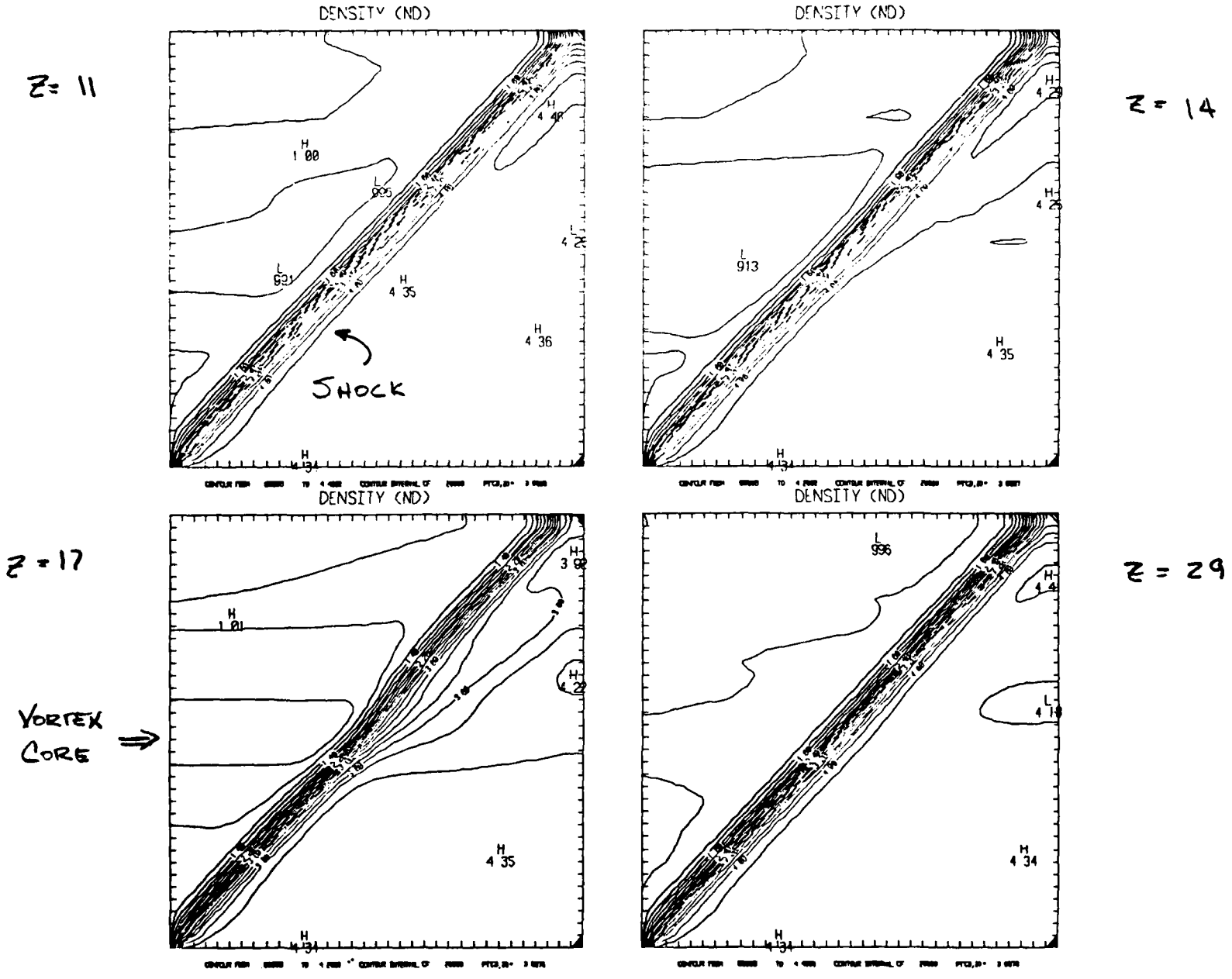

MS XY 11 4 17 2

XZ FACE

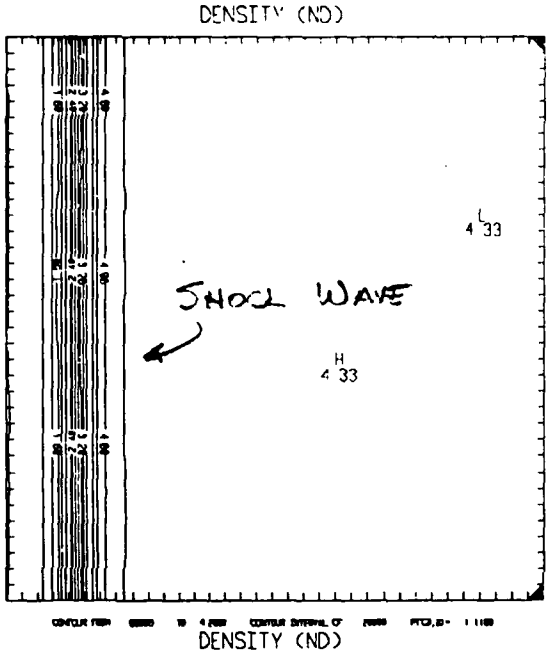

Y = 6

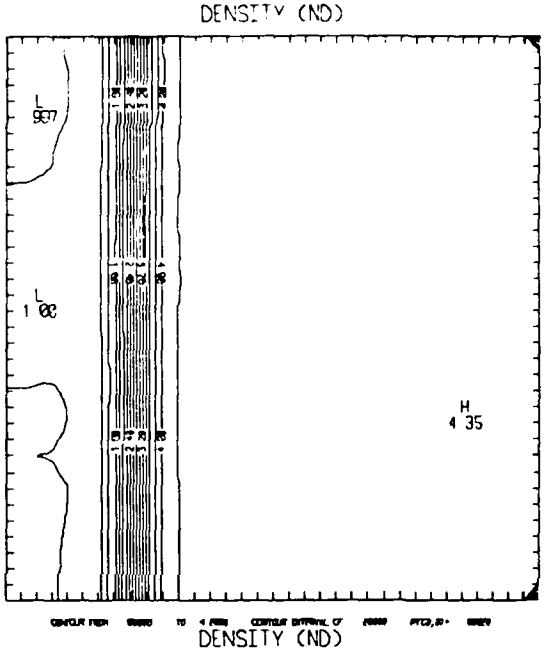

Y = 10

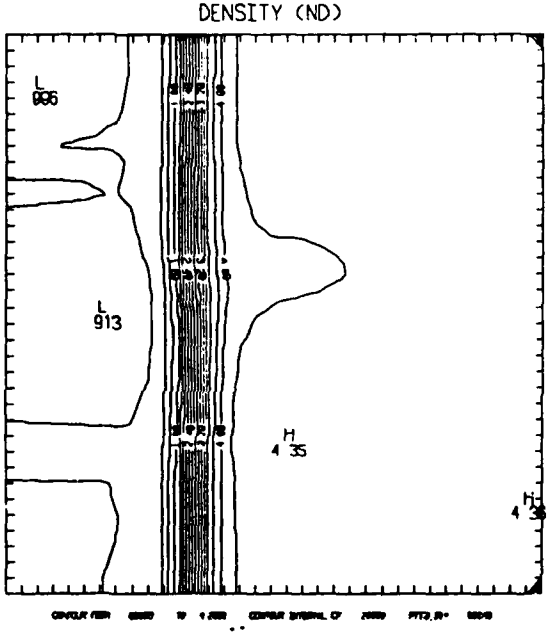

Y = 14

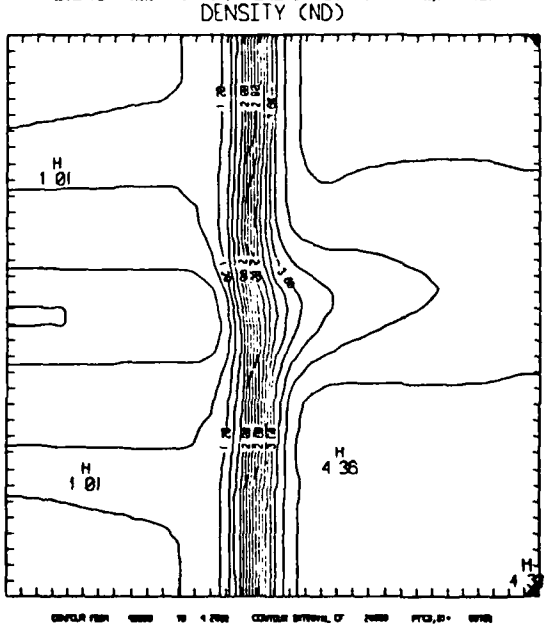

Y = 18

VORTEX CORE

(3) 1 0 1 9 ZX S1-1

XZ FACE

Y = 22

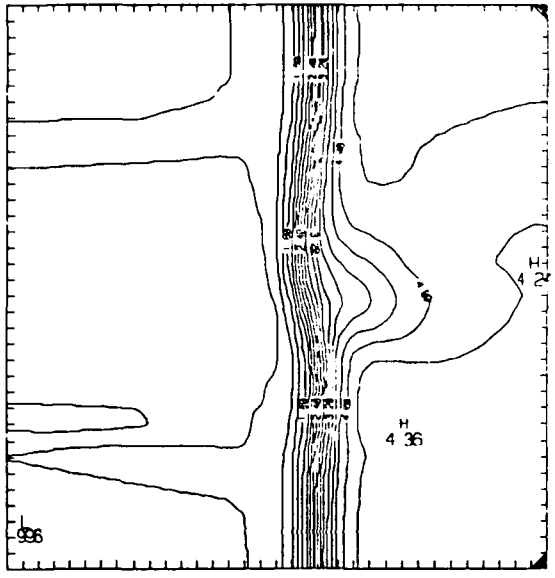

Y = 26

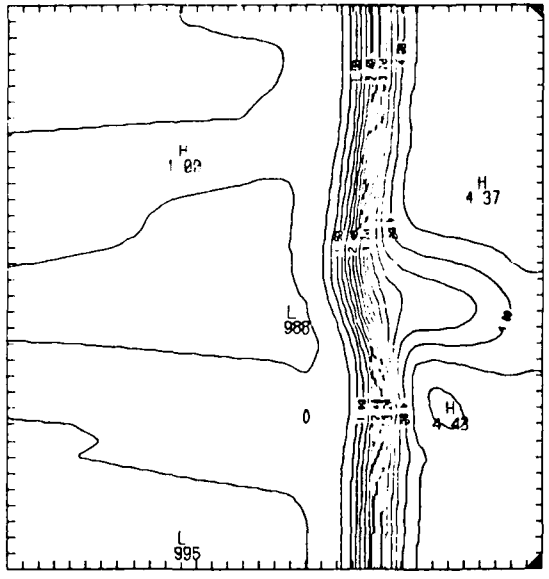

Y = 30

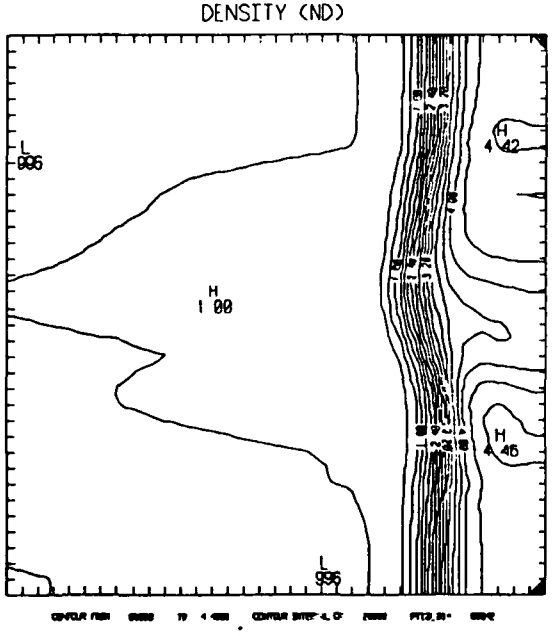

Y = 34

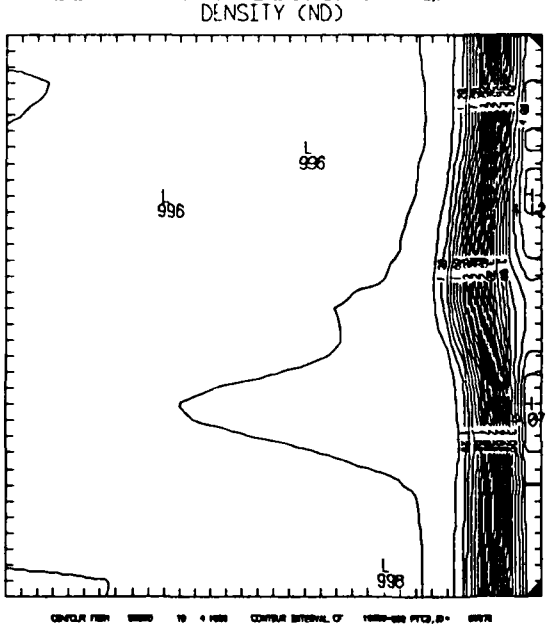

M 5
XZ 22 26 30

IV. CONCLUSION

The Fellowship Program in Hypersonic Aerodynamics sponsored at the University of Maryland by ARO has been very productive, far beyond its initial scope. The work of two exceptional Ph.D. students is summarized in this report. A similar fellowship program (now involving one Ph.D. student) is currently in progress, and will be reported at the proper time.

END

DATED

FILM

8-88

DTIC